Cell Reports

The adhesion G-protein-coupled receptor *mayo/CG11318* controls midgut development in *Drosophila*

Graphical abstract

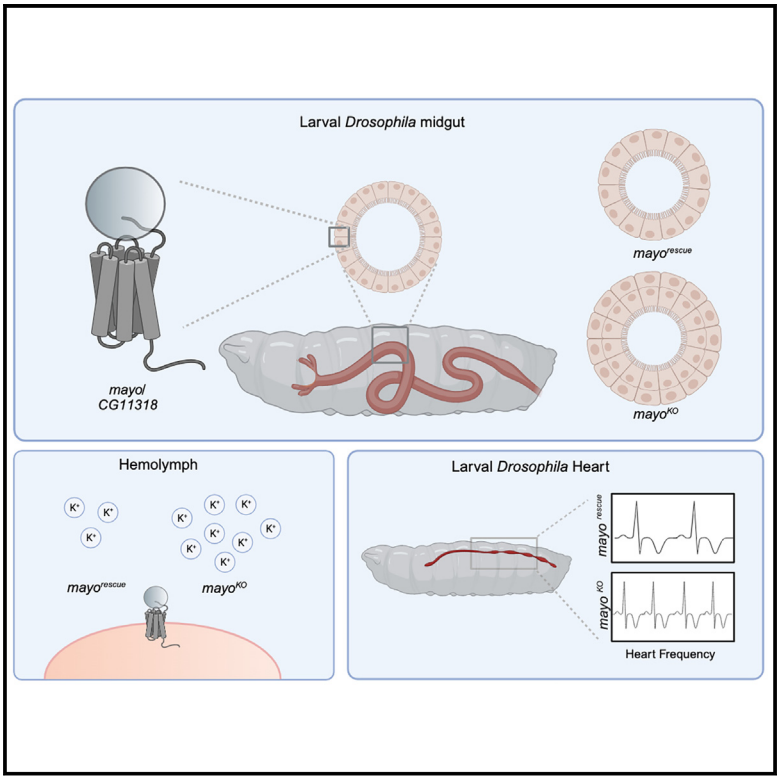

Authors

Fernando Vieira Contreras, Genevieve M. Auger, Lena Müller, ..., Dmitrij Ljaschenko, Beatriz Blanco-Redondo, Tobias Langenhan

Correspondence

beatriz.blanco-redondo@medizin.uni-leipzig.de (B.B.-R.), tobias.langenhan@gmail.com (T.L.)

In brief

Vieira Contreras et al. reveal how the *Drosophila* adhesion G-protein-coupled receptor *mayo* impacts midgut development through enterocyte proliferation. *mayo* contributes to the potassium homeostasis in the hemolymph and thereby non-cell-autonomously controls cardiac frequency.

Highlights

- The *CG11318* locus encodes the adhesion GPCR *mayo*
- *mayo* controls midgut size through enterocyte proliferation
- *mayo* removal results in hyperkalemia
- Loss of *mayo* causes tachycardia

Vieira Contreras et al., 2024, Cell Reports *43*, 113640
January 23, 2024
https://doi.org/10.1016/j.celrep.2023.113640

CellPress

Cell Reports

CellPress
OPEN ACCESS

Report

The adhesion G-protein-coupled receptor *mayo/CG11318* controls midgut development in *Drosophila*

Fernando Vieira Contreras,[1,6] Genevieve M. Auger,[1,6] Lena Müller,[1] Vincent Richter,[2] Wolf Huetteroth,[2] Florian Seufert,[3] Peter W. Hildebrand,[3] Nicole Scholz,[1] Andreas S. Thum,[2] Dmitrij Ljaschenko,[1] Beatriz Blanco-Redondo,[1,*] and Tobias Langenhan[1,4,5,7,*]

[1]Rudolf Schönheimer Institute of Biochemistry, Division of General Biochemistry, Medical Faculty, Leipzig University, Johannisallee 30, 04103 Leipzig, Germany
[2]Institute of Biology, Department of Genetics, Faculty of Life Sciences, Leipzig University, Talstraße 33, 04103 Leipzig, Germany
[3]Institute for Medical Physics and Biophysics, Medical Faculty, Leipzig University, Härtelstrasse 16-18, 04107 Leipzig, Germany
[4]Institute of Biology, Faculty of Life Sciences, Leipzig University, Talstraße 33, 04103 Leipzig, Germany
[5]Comprehensive Cancer Center Central Germany (CCCG), Germany
[6]These authors contributed equally
[7]Lead contact
*Correspondence: beatriz.blanco-redondo@medizin.uni-leipzig.de (B.B.-R.), tobias.langenhan@gmail.com (T.L.)
https://doi.org/10.1016/j.celrep.2023.113640

SUMMARY

Adhesion G-protein-coupled receptors (aGPCRs) form a large family of cell surface molecules with versatile tasks in organ development. Many aGPCRs still await their functional and pharmacological deorphanization. Here, we characterized the orphan aGPCR *CG11318/mayo* of *Drosophila melanogaster* and found it expressed in specific regions of the gastrointestinal canal and anal plates, epithelial specializations that control ion homeostasis. Genetic removal of *mayo* results in tachycardia, which is caused by hyperkalemia of the larval hemolymph. The hyperkalemic effect can be mimicked by a raise in ambient potassium concentration, while normal potassium levels in *mayo*^{KO} mutants can be restored by pharmacological inhibition of potassium channels. Intriguingly, hyperkalemia and tachycardia are caused non-cell autonomously through *mayo*-dependent control of enterocyte proliferation in the larval midgut, which is the primary function of this aGPCR. These findings characterize the ancestral aGPCR Mayo as a homeostatic regulator of gut development.

INTRODUCTION

The gastrointestinal (GI) tracts in *Drosophila* and vertebrate species share features of anatomical and functional compartmentalization. The foregut (equivalent to the mammalian esophagus) passes ingested food to the crop (stomach), the anterior midgut (small intestine) controls nutrient, ion, and water absorption, and, finally, the hindgut (large intestine) is involved in electrolyte reabsorption from the Malpighian tubules (equivalent to the kidney in mammals).[1–4] Instead of the crypt-villus structure found in mammals, the *Drosophila* midgut consists of a monolayer populated by different cell types. Before pupation, the larval midgut is composed of enterocytes (ECs), which derive from principal midgut epithelial cells (PMECs), interstitial cell precursors (ICPs), and adult midgut precursors (AMPs), which generate and are enveloped by peripheral cells (PCs). AMPs are also thought to give rise to enteroendocrine cells (EEs; Figure 4A).[5] The larval AMPs, ensheathed by PCs, constitute a stem cell niche for transient pupal midgut development until metamorphosis and also the generation of the adult midgut.[6–8] Dysregulation of midgut cell proliferation can lead to malabsorption of nutrients and defective ion homeostasis.[9–12]

Adhesion G-protein-coupled receptors (aGPCRs) are a large group of surface sensors with various functions in tissue development. For example, aGPCRs exert control of vital aspects of embryogenesis and cardiogenesis, as well as nervous and immune systems development.[13] Genetic dysfunctions of aGPCRs are associated with various human pathologies such as multiple cancers,[14,15] neurodevelopmental disorders,[16–18] and immune defects.[19,20] Five aGPCR homologs have been identified in *Drosophila* to date,[21] but only two of them have been characterized in depth: the ADGRL/E homolog *Latrophilin/Cirl/CG8639* and the ADGRC receptor *CELSR/Flamingo/Starry night/CG11895*. *CG15744/remoulade* is an ADGRA-like receptor. *CG11318* and *CG15556*, which we termed *mayo* and *ketchup*, respectively, are ancestral aGPCRs with equidistant homology to all vertebrate aGPCR subfamilies.[21] Here, we found that *mayo* plays a role in the development of the larval midgut and non-cell-autonomously inflicts tachycardia in *mayo*^{KO} larvae, linking the operations of the GI and cardiovascular systems.

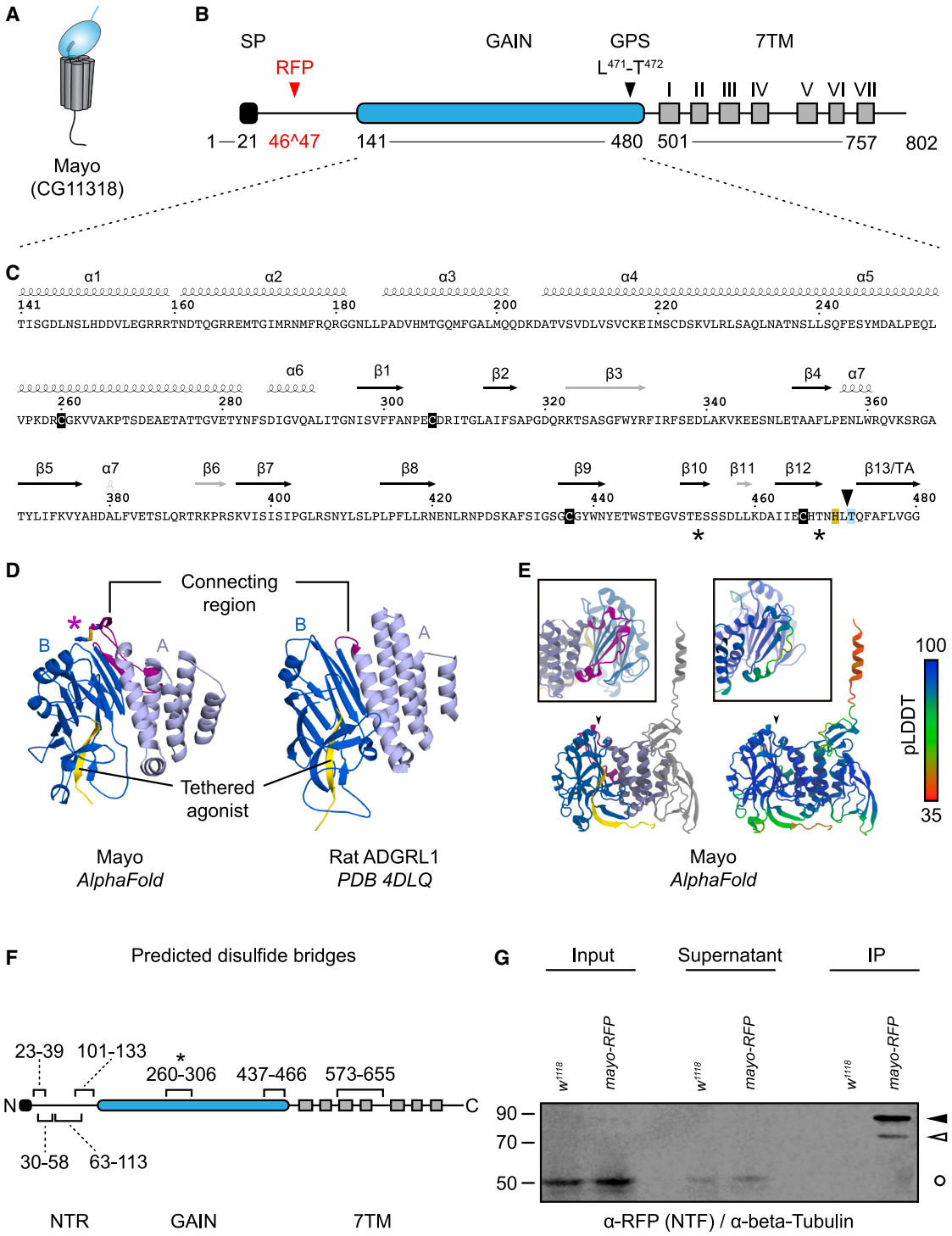

Figure 1. Mayo is a primordial adhesion GPCR

(A) Domain composition of the aGPCR Mayo.

(B) Domain boundaries are indicated below the model. Transmembrane helices (roman numerals), GPS (GPCR proteolysis site) indicated by a black arrowhead. Location of the RFP insertion in the Mayo protein indicated by red arrowhead. SP, signal peptide. Based on UniProt: Q8SZ78.

(C) Secondary structure prediction of the Mayo GAIN domain by Phyre2. Positions of α-helices and β-sheets are indicated above the amino acid sequence. The numbering corresponds to the initial fold model from Araç et al.,[26] and elements with low support are in gray. Bridged cysteines are boxed in black, positions of

(legend continued on next page)

RESULTS

The *CG11318* locus encodes the aGPCR *mayo*

A phylogenetic survey of the *Drosophila melanogaster* genome showed that the *CG11318* locus contains an aGPCR-encoding gene with no apparent similarity to any of the known nine aGPCR subfamilies.[21] We named this gene *mayo*. Together with the syntenic locus *CG15556/ketchup*, *mayo* forms a primordial subfamily within the aGPCR family of GPCRs. We modeled the protein domain layout of the *mayo* gene product using the Phyre2[22] and PSIPRED[23] servers and *de novo* through AlphaFoldDB[24] followed by protein structure search by FoldSeek.[25] This approach indicated a simple receptor layout containing only an extracellular GPCR autoproteolysis-inducing (GAIN) domain and a heptahelical transmembrane domain with high confidence (Figures 1A and 1B).

Secondary structure prediction of the Mayo GAIN domain provided overall support for the fold model based on X-ray crystallographic studies (Figure 1C).[26] In addition, AlphaFold predictions of the Mayo GAIN domain show very good agreement with solved GAIN domain crystal structures (Figure 1D) and high pLDDT (predicted local distance difference test) values (Figure 1E).[24] A main difference of the published GAIN domain structures concerns the region connecting subdomains A and B (residues 254–288), which forms a short helical segment (^{271}EAETATT^{277}), and an additional β-sheet comprising the most N-terminal element of the subdomain B beta sandwich (^{280}ETYNF^{284}), whereas this segment is disordered in known GAIN domains (Figure 1E). The prediction of four disulfide bonds in the N-terminal region (NTR) of the receptor preceding the GAIN domain suggests the presence of structured regions (Figure 1F); however, no reasonable matches were obtained. In addition, while the majority of GAIN domains contain two pairs of cysteines forming β9-β12 and β11-β12 bridges in subdomain B, the GAIN domain of Mayo lacks the latter pair (Figure 1F). Instead, it contains a unique disulfide bridge between the start of the connecting region and the β1-β2 loop (Figures 1D and 1F).

Due to these structural differences, we investigated if the Mayo GAIN domain permits autoproteolysis at a conserved GPCR proteolysis site (GPS), a biochemical hallmark of aGPCRs and relevant post-translational processing events in receptor maturation, membrane transport, and signaling.[27,28] We utilized a genomic engineering platform and φC31-assisted transgene integration to insert modified genomic transgenes at an *attP* landing site, which had replaced the *mayo* gene (Figure S1A). This strategy ensures physiological *cis*-regulatory expression control from each modified *mayo* allele.[29] At first, we generated a fly strain that contained a monomeric RFP (red fluorescent protein) domain inserted in frame in the NTR of Mayo (*mayo-RFP*) (Figure 1B). We immunoprecipitated protein extracts obtained from transgenic *mayo-RFP* pupae with an α-RFP antiserum and detected two specific bands that correspond in size to the full-length receptor fusion protein (~114 kDa) and its N-terminal fragment truncated at the GPS (~77 kDa) (Figure 1G). This finding supports results of suppressed GAIN domain cleavage through mutagenesis in Mayo-NRS-LexA proteins[30] and suggests that Mayo is autoproteolytically processed despite the structural peculiarities of its GAIN domain. This renders Mayo a primordial aGPCR, albeit with similar molecular and biochemical characteristics to phylogenetically younger aGPCRs.

Loss of *mayo* causes tachycardia

In order to specify the physiological role of *mayo*, we examined previously engineered $mayo^{KO}$ animals[29] in comparison to $mayo^{rescue}$ flies, a strain in which the removed *mayo* locus was reintegrated through φC31-mediated transgenesis. No overt developmental delay or defects of $mayo^{KO}$ animals were observed. However, we noticed that third-instar $mayo^{KO}$ larvae displayed an accelerated heart rate. Kymographic analysis of cardiac activity video recordings in intact $mayo^{KO}$ L3 larvae (Figure 2A) confirmed an increase in cardiac frequency by 30.9% (169.6 ± 4.1 beats per minute [BPM], n = 30; data as mean ± standard error of the mean [SEM]) compared to $mayo^{rescue}$ controls (129.6 ± 2.2 BPM, n = 30; Figure S1B). For the expedited analysis of cardiac frequencies, we also visually counted heart-pumping events, obtaining similar results ($mayo^{rescue}$: 139.7 ± 4.0 BPM; $mayo^{KO}$: 180.7 ± 3.1 BPM; 29.4% increase; Figure 2B). Thus, we henceforth used this method for subsequent quantifications and presented heart rates observed in experimental genotypes normalized to appropriate wild-type controls.

Tachycardic frequencies were also observed in *trans*-heterozygous larvae that carried the $mayo^{KO}$ allele in *trans* to the small deficiency *Df(3R)Exel7379*, which uncovers the *mayo* locus, confirming that the changes in the heart rate originate from loss of *mayo* (Figure S1C). Interestingly, when we examined the impact of *mayo* gene dosage on the larval heart rate, we observed that heterozygous larvae carrying a $mayo^{rescue}$ and a $mayo^{KO}$ allele in *trans* displayed an intermediate heart rate compared to the homozygous control animals (Figure S1D). This haploinsufficiency suggests that the function of the *mayo* gene product critically scales with its amount.

missing bridged cysteines in the Mayo GAIN domain are indicated by asterisks, the GPS is shown by an arrowhead, and GPS flanking residues relevant for self-cleavage (−2, +1) are colored.

(D) Comparison of the GAIN domains of Mayo (predicted; aa 142–490) and rADGRL1 (PDB: 4DLQ). Structural differences in connecting regions are highlighted in purple, and the asterisk highlights a non-conserved disulfide bridge (C260-C306) shown as licorice. Light blue, subdomain A; blue, subdomain B; yellow, tethered agonist (*Stachel*).

(E) pLDDT confidence score for AlphaFold prediction of the entire Mayo ECD (aa 1–490). Connecting region is highlighted by a box. pLDDT values over 70 are considered "confident."

(F) Position of AlphaFold-predicted disulfide bridges in Mayo. Four are located in the N-terminal region (NTR; aa 22–141), and GAIN domain contains a conserved (C437-C466) and a non-conserved disulfide bridge (C260-C306; asterisk).

(G) α-RFP co-immunoprecipitation of Mayo-RFP of indicated genotype showing full-length receptor (closed arrowhead) and its NTF generated by GAIN autocleavage (open arrowhead). β-Tubulin served as a loading control (circle). Note that the minimum displayed brightness value of the blot was increased to 136% using ImageJ.

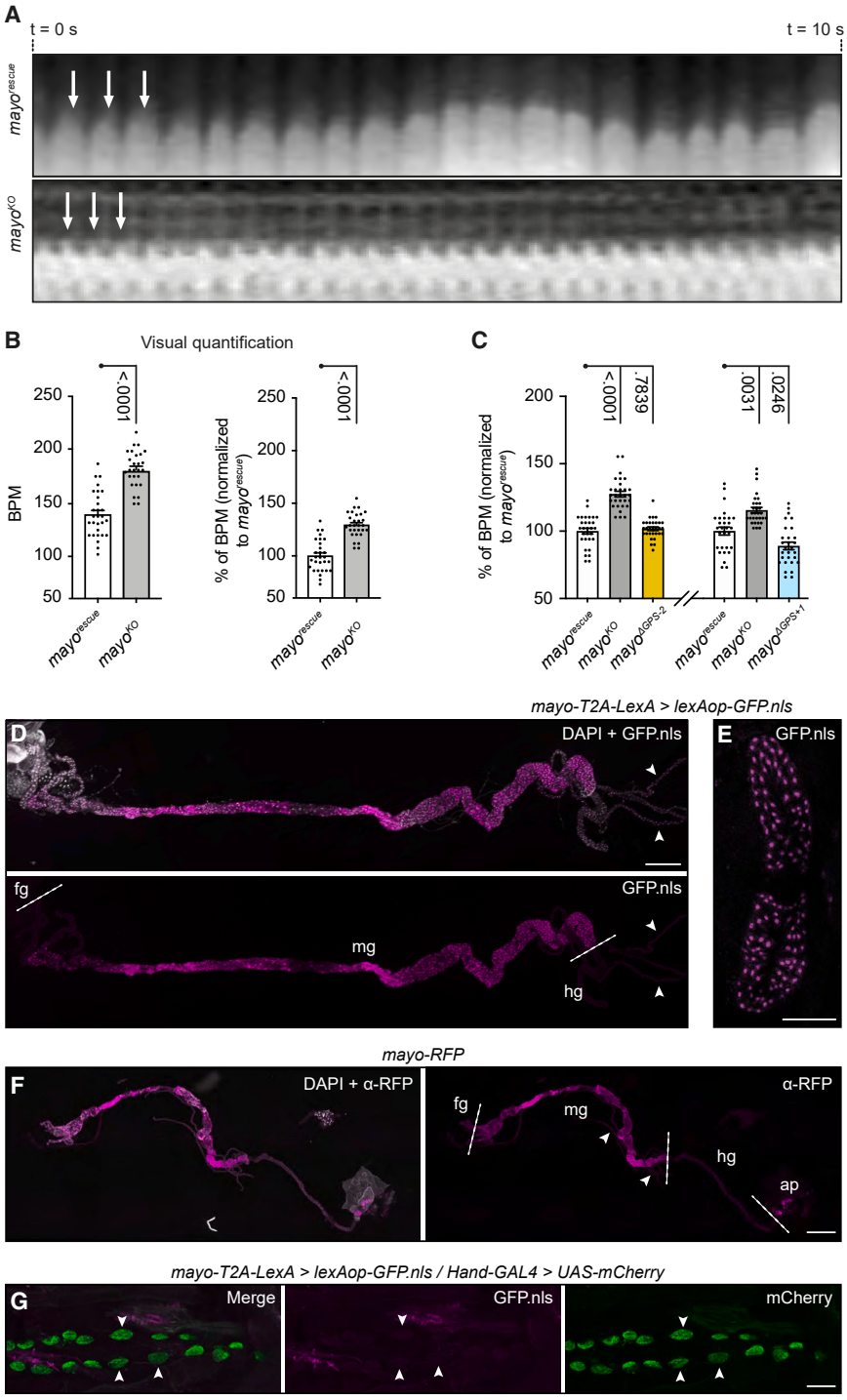

Figure 2. *mayo* controls cardiac activity but is not expressed in the larval heart

(A) 10 s period kymographs of cardiac activity of *mayo*^{rescue} and *mayo*^{KO} L3 larvae show increased heart pace in the mutants. Individual contractions are indicated by white arrows.

(B) Visual quantitative assessment of cardiac frequency shows increase of heart rate in *mayo*^{KO} mutants (absolute left, normalized right). See also Figure S1B.

(C) Cardiac frequency assays of L3 larvae show that GAIN domain proteolysis suppression on the N-terminal side of the GPS does not result in *mayo* dysfunction (*mayo*$^{\Delta GPS-2}$), while a point mutation of the C-terminal GPS residue and putative tethered agonist sequence of the receptor results in mildly lower frequencies (*mayo*$^{\Delta GPS+1}$). Left and right assays were performed separately.

(D) Dissected gastrointestinal canal of a third-instar larva expressing *lexAop-GFP.nls* marker (magenta) under control of a transcriptional *mayo-T2A-LexA* driver shows expression in the midgut (mg) but no other parts of the alimentary canal including the foregut (fg), hindgut (hg), and Malpighian tubules (arrowheads). Dashed lines indicate the anterior and posterior borders of the midgut. DAPI was used as counterstain. Scale bar: 500 μm.

(E) The epithelium of the anal pads shows strong *mayo* expression. Scale bar: 100 μm.

(F) Immunohistochemical staining of the gastrointestinal tract of *mayo-RFP* larvae corroborates expression of Mayo in the midgut (mg) and anal pad (ap) but not in the fg, hg, or Malpighian tubules (arrowheads). Dashed lines indicate the anterior and posterior borders of the midgut. DAPI was used as counterstain. Scale bar: 500 μm.

(G) *mayo-T2A-LexA* is not expressed in the larval heart. Pericardial nephrocytes marked with *Hand-GAL4* (green, arrowheads) outline the cardiac tube. Scale bar: 100 μm. Data are shown as mean ± SEM.

We harnessed the larval tachycardia phenotype to assess how autoproteolytic processing of Mayo through its GAIN domain, the tell-tale domain of aGPCRs,[26] impacts its molecular function. We generated *mayo* alleles (*mayo*$^{\Delta GPS-2}$, *mayo*$^{\Delta GPS+1}$) in which GAIN domain self-cleavage was suppressed through alanine replacement of the residues at the −2 (His) and +1 (Thr) positions of the GPS (Figure 1C), respectively[30] (Figure S1E). Interestingly, we observed that suppression of receptor self-cleavage at the −2 position to the GPS did not result in any notable heart rate differences when compared to wild-type animals (Figure 2C). GPS mutagenesis of the +1 GPS residue, however, showed a mild but significant reduction in cardiac frequency (Figure 2C). As both GPS mutations inhibit GAIN domain cleavage and subsequent N-terminal fragment (NTF) release in a similar way, these effects are likely not responsible for the lower heart rates of *mayo*$^{\Delta GPS+1}$ animals. Instead, +1 GPS mutagenesis changes, in addition to its autoproteolysis-supporting role, the most N-terminal residue of the putative tethered agonist (TA) sequence of Mayo (Figure 1C), which may impact metabotropic signaling of the Mayo receptor.

mayo is expressed in the larval midgut and anal pad organs

To account for the cardiac phenotypes, we next reassessed the expression of *mayo* in more detail. Previously, we found activity of *mayo-p-GAL4*, a transcriptional reporter transgene that expresses GAL4 from the endogenous *mayo* promoter, in parts of the gut and the anal pad of third-instar larvae. We found no expression in the heart or any other tissue, including the nervous system,[29] which is also supported by single-cell RNA sequencing (RNA-seq) datasets of the larval brain[31] and transcriptome analyses of fly tissue.[32] We used an independent *mayo-T2A-LexA* translational reporter[33] and confirmed that it was identically expressed as *mayo-p-GAL4* in the midgut section of the alimentary canal (Figure 2D) and in the anal pads (Figure 2E), which partake in ion and water homeostasis (Figure 2E). We also investigated *mayo-RFP* larvae for the analysis of Mayo protein expression. First, we determined that RFP insertion into the potentially structured NTR of Mayo (Figures 1B and 1F) did not result in cardiac frequency abnormalities when compared to $mayo^{rescue}$ animals (Figure S1F). Immunohistochemical analysis of Mayo-RFP using an α-RFP antiserum confirmed expression in the larval midgut and the anal pad epithelium (Figure 2F), while fluorescent Mayo-RFP signals were too low for detection.

Interestingly, we did not find *mayo-p-GAL4* expression, *mayo-T2A-LexA* activity, or Mayo-RFP signals in heart cells or cells of the excretory system such as the Malpighian tubules (Figures 2D and 2F). Given the increased cardiac frequency of $mayo^{KO}$ mutants, we used suitable markers to evaluate whether *mayo* may be expressed at low levels in the constituent cells of the larval heart, i.e., cardiomyocytes and pericardial nephrocytes. We employed a GAL4 reporter driven by the *Hand* promoter,[34,35] a transcription factor involved in cardiogenesis[36,37] that is strongly expressed in pericardial nephrocytes and cardioblasts.[38,39] When co-expressed with a cardiac reporter, *mayo-T2A-LexA* could not be co-detected with *Hand-GAL4* (Figure 2G), indicating that *mayo* is not endogenously present in the larval heart. Our data thus indicate that *mayo* impacts the larval heart rate non-cell autonomously.

mayo removal results in hyperkalemia

In addition to heart-autonomous parameters, the cardiac frequency can be regulated through heart-non-autonomous factors. This encompasses the systemic extracellular ion composition, which governs cardiomyocyte excitability throughout the cardiac cycle and its pacing.[40] Further, interference with transmembrane K^+, but not Ca^{2+} or Na^+, currents causes tachycardia in *Drosophila*.[41–43]

Therefore, we next tested how alterations in the extracellular ion concentration affect $mayo^{rescue}$ and $mayo^{KO}$ animals. We determined the heart rate of individual third-instar larvae before and after exposure to 1.8 M KCl solution. While $mayo^{KO}$ mutants did not display changes in cardiac frequency, elevation of extracellular KCl levels resulted in a marked tachycardic effect in $mayo^{rescue}$ animals, phenocopying the loss of *mayo* (Figure 3A). In contrast, exposure to 2.0 M NaCl solution did not affect either $mayo^{rescue}$ or $mayo^{KO}$ larvae (Figure 3B). This suggested that maintenance problems of extracellular K^+ concentration may underlie the cardiac effects in $mayo^{KO}$ mutants.

To corroborate this assumption, we used the voltage-gated potassium channel (VGKC) blocker 4-aminopyridine (4-AP)[44] to inhibit fast K^+ currents in $mayo^{rescue}$ and $mayo^{KO}$ animals. Comparison of heart rates upon incubation with the drug showed that $mayo^{KO}$-associated tachycardia was rescued at a blocking concentration of 0.2 mM (Figure 3C), but not under 0.02 mM 4-AP (Figure S2A), while 4-AP had no effect on $mayo^{rescue}$ larvae. Conversely, inhibition of voltage-gated sodium channels (VGNCs) via tetrodotoxin (TTX)[40] across three log units did not affect cardiac function in larvae irrespective of the presence or absence of *mayo* (Figures 3D and S2B). This further supports that K^+ drives the tachycardia in $mayo^{KO}$ mutants.

As *mayo* is unlikely to impact cardiac VGKCs directly due to its absence from cardiomyocytes (Figure 2G), loss of *mayo* may affect the extracellular K^+ concentration in the hemolymph, the major extracellular fluid in insects. In order to test this assumption, we collected hemolymph samples from individual larvae and determined their osmolality. However, no significant difference was found between $mayo^{rescue}$ (269 ± 6 mOsm/kg; n = 30 animals) and $mayo^{KO}$ (283 ± 7 mOsm/kg; n = 30 animals) animals, suggesting that the overall ion composition of the hemolymph is unperturbed in $mayo^{KO}$ larvae (Figure 3E).

To directly assess the extracellular K^+ concentration ($[K^+]_{ex}$) in the hemolymph, we established measurements using K^+-selective electrodes. We punctured the cuticle of the larvae, which causes a drop of hemolymph to leak out of the body cavity. A K^+-selective and a reference electrode were immediately dipped into the drop, and the potential between the two was recorded (Figure 3F). Each K^+-selective electrode was calibrated with solutions of increasing K^+ concentration before use (Figure 3G). Via this approach, we determined the hemolymph $[K^+]_{ex}$ concentration of $mayo^{rescue}$ larvae at 8.0 ± 0.5 mM (n = 16 animals; range: 4.5 to 12.1 mM; Figure 3H), which is in good agreement with previous measurements.[45,46] Intriguingly, the $mayo^{KO}$ hemolymph displayed a significantly increased average K^+ concentration of 9.4 ± 0.5 mM (n = 14 animals; range: 6.3 to 12.6 mM; Figure 3H). Calculation of the Nernst potential for K^+ found an increased K^+ equilibrium potential for $mayo^{KO}$ animals (−56.5 ± 1.3 mV; range: −66.2 to −48.7 mV) compared to $mayo^{rescue}$ controls (−60.8 ± 1.6 mV; range: −74.6 to −49.7 mV), which is in line with previous experimental findings in larval cardiomyocytes estimating that a log unit change in $[K^+]_{ex}$ results in a resting membrane potential shift by 57 mV.[42] Subtle differences in K^+ homeostasis strongly affect the slow diastolic depolarization of cardiomyocytes, which governs their automatic activity and mainly carried by K^+.[42] Together with the pharmacological findings, we conclude that hyperkalemia in larval hemolymph accounts for the tachycardic effects associated with loss of *mayo*.

mayo is required in midgut PCs and ECs to regulate larval heart rate

In order to establish which organs and cell types require *mayo* to regulate hemolymph K^+ levels, we assayed the heart rate in larvae upon RNAi-mediated suppression of *mayo* in its endogenous expression sites, the midgut and anal pad. Both show transcriptional and translational expression of *mayo* reporters (Figures 2D and 2E; Blanco-Redondo and Langenhan[29]) and partake in ion and water homeostasis. We first evaluated two fly strains

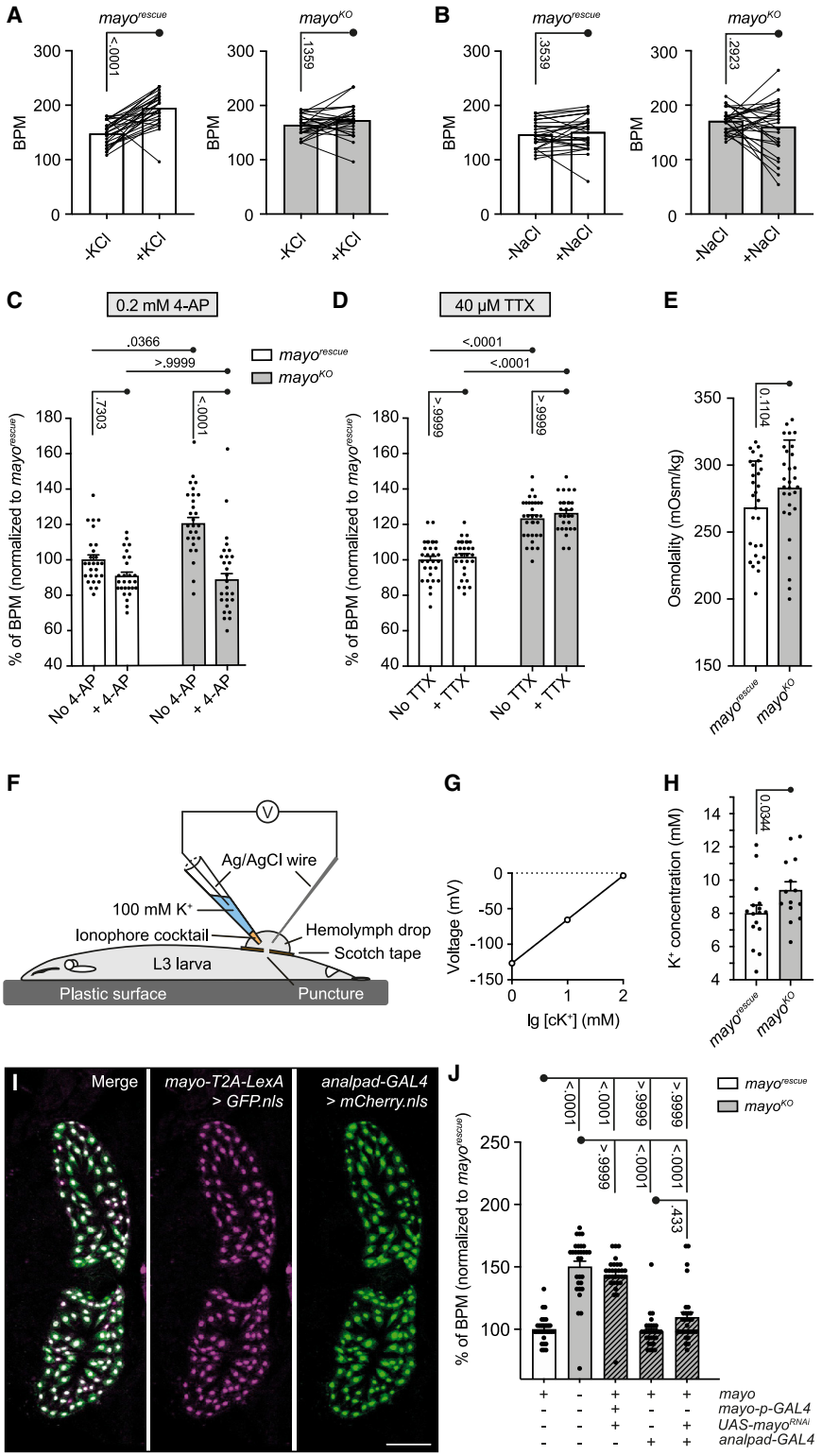

Figure 3. *mayo* regulates hemolymph potassium concentration

(A and B) Increased environmental K^+ concentration results in tachycardia in wild-type animals and phenocopies $mayo^{KO}$. Plotted are heart rates of individual larvae before and during exposure to elevated potassium (KCl) (A) or sodium (NaCl) (B) concentrations.

(C and D) Cardiac frequency measurements upon inhibition of voltage-gated potassium channels by 4-AP (C) and voltage-gated sodium channels by TTX (D) show rescue of the tachycardia phenotype in $mayo^{KO}$ larvae under 4-AP treatment. See also Figures S2A and S2B.

(E) $mayo^{rescue}$ and $mayo^{KO}$ larvae have similar hemolymph osmolalities.

(F) Schematic of the setup used to measure the hemolymph K^+ concentration. Please note that the Scotch tape covered the entire body of the larva, taping it to the surface.

(G) Calibration curve of the K^+-selective electrode.

(H) The hemolymph of $mayo^{KO}$ larvae contains increased $[K^+]_{ex}$.

(I) *analpad-GAL4* (green) overlaps with the *mayo* expression pattern in the anal pad. Co-expression with *mayo-T2A-LexA* (magenta) is shown. Anterior to the left. Scale bar: 100 µm. See also Figure S3D.

(J) Cardiac frequency is unperturbed after *mayo* knockdown in the anal pad. See also Figures S3A and S3B.

All data are shown as mean ± SEM.

carrying *UAS-RNAi* constructs that target *mayo* transcripts (*P{GD705}*^{v3395}; *P{KK105668}*^{v108136})[47] for their ability to induce tachycardia in wild-type larvae when crossed to the *mayo-p-GAL4* driver and selected the most potent one (*P{GD705}*^{v3395}; redesignated as *UAS-mayo*^{RNAi}) for further analyses (Figure S3A). We next evaluated potential off-target effects of *UAS-mayo*^{RNAi} by constructing a fly strain in which we deleted the *mayo* open reading frame from the *mayo-p-GAL4* transgene to allow for *mayo-p-GAL4* activation without Mayo expression (*mayo*^{KO}*-p-GAL4*). *mayo-p-GAL4* and *mayo*^{KO}*-p-GAL4* expression patterns were indistinguishable (Figure S3B). When *UAS-mayo*^{RNAi} was expressed by *mayo*^{KO}*-p-GAL4* in *mayo*^{KO} background, no additional effect on heart rate or other abnormalities were noted in comparison to *mayo*^{KO} larvae (Figure S3C). Collectively, *GAL4*-dependent knockdown by *UAS-mayo*^{RNAi} specifically and sufficiently removes *mayo* function.

To examine the consequences of *mayo* removal from the anal pads, we screened the Vienna tile library for *enhancer-GAL4* drivers[48] that selectively express in the anal pad organ and identified *VT050217-GAL4*, which we termed *analpad-GAL4* (Figures 3I and S3D). Knockdown of *mayo* by *analpad-GAL4* did not affect cardiac activity (Figure 3J).

The larval midgut is generated from a common endodermal precursor cell population and gives rise to three different cell lineages (Figure 4A)[5]: PMECs, ICPs, and AMPs. PMECs differentiate into ECs (*myosin-GAL4*$^{+}$ or *mex-GAL4*$^{+}$; Jiang and Edgar,[49] Huang et al.,[50] and Phillips and Thomas[51]) that form the midgut epithelium, while ICPs and AMPs migrate and make contact with the extracellular matrix.[52] The AMPs (*delta-GAL4*$^{+}$; Mathur et al.[6]) locally proliferate and generate a transient stem cell niche by spawning off PCs (*Su(H)GBE-GAL4*$^{+}$; Mathur et al.[6]), which enwrap AMP nests and hold them in an undifferentiated state until metamorphosis.[6] Some AMPs differentiate into EEs (*prospero-GAL4*$^{+}$; Takashima et al.[53]) in the larva and become integrated into the future transient pupal midgut.[5,53] We observed that *mayo* knockdown in AMPs (Figure S3E) and EEs (Figure S3F) did not impact cardiac pacing, but suppression of *mayo* expression by RNAi in PCs (Figure 4B) and ECs (Figures 4C and S3G) resulted in increased heart frequencies of larvae. Therefore, *mayo* is required in PCs and ECs for physiological cardiac pacing.

We also reconfirmed that *mayo* is not expressed and does not operate in the larval heart using the RNAi approach. No effects on heart rate were noted when *mayo* knockdown was directed to myocytes including cardiomyocytes (*Mef2-GAL4*$^{+}$; Figure S3H; Bour et al.[34] and Dreschler et al.[35]) and pericardial nephrocytes (*dorothy-GAL4*$^{+}$; Kimbrell et al.[54]; Figure S3I) or in cardioblasts during patterning of the larval heart by expression of *tin-GAL4* (Figure S3J), an NK-2 homeobox family member necessary for mesoderm development.[55]

mayo controls midgut size through EC proliferation

As PCs and ECs control hemolymph potassium levels *mayo* dependently, we investigated these cell lineages further. Co-expression of *mayo-T2A-LexA* with the larval enteric lineage GAL4 markers confirmed that *mayo* is present in PCs (*Su(H)GBE-GAL4*) and ECs (*myosin-GAL4*) but not in AMPs (*delta-GAL4*) or EEs (*prospero-GAL4*) (Figures 4D and 4E).

This suggests that *mayo* acts during cell-fate transition between principal midgut precursor cells (PMECs; Figure 4A) and ECs (Figure 4A), where it could partake in the regulation of the EC pool. To test this assumption, we quantified the number of *mayo-p-GAL4*$^{+}$ cells in *mayo*^{rescue} and *mayo*^{KO} L3-stage larval midguts. We found that loss of *mayo* results in an increased number of *mayo-p-GAL4*$^{+}$ cells (Figure 4F), while the cell size was unaffected by loss of *mayo* (Figure 4G). To clarify the identity of the expanded cell pool in *mayo*^{KO} larvae, we obtained lineage-specific cell counts of *mayo*-expressing cells. This revealed that only the larval *myosin-GAL4*$^{+}$ EC lineage was enlarged (Figure 4H), while the number of *Su(H)GBE-GAL4*$^{+}$ PCs between *mayo*^{rescue} and *mayo*^{KO} animals was indistinguishable (Figure 4I). Also, the number of *prospero-GAL4*$^{+}$ *mayo*$^{-}$ AMP-derived larval EEs was unchanged in *mayo*^{KO} larval midguts (Figure 4J). This suggests that *mayo* is physiologically required to cap the number of ECs in early-L3-stage larvae. Interestingly, when we compared the length of dissected GI tracts of adult flies, we found that *mayo*^{KO} animals displayed elongated guts, indicating a post-pupation role for *mayo* in the control of adult gut development as well (Figures 4K–4M).

In sum, this indicates that systemic L3 potassium levels correlate with the number of ECs in the larval midgut, which depend on the function of *mayo*. Thus, the increase in EC number may underlie the increase of K^+ in the hemolymph of *mayo*^{KO} animals.

DISCUSSION

Despite its basal phylogenetic position in the aGPCR family[21] and its simple molecular layout, Mayo displays structural and functional hallmarks of aGPCRs including a 7TM domain that likely can couple to G proteins and other second messenger routes similar to other aGPCRs.[27,56] Mayo also contains a GAIN domain, which can be autoproteolytically processed. This implies that Mayo shares important biochemical properties with the rest of the structurally diverse aGPCR family[27,56,57] and operates similarly to other aGPCRs. This assumption is based on the role for GAIN domain proteolysis in aGPCR signal transduction initiated by ligand engagement and/or mechanical strain.[30,58–61] According to the dissociation signaling paradigm, aGPCR separation is necessary for the exposure of a cryptic TA (*Stachel*), which is concealed within the GAIN domain before its separation.[57,62–66] Thus, self-cleavage of Mayo is a prerequisite for its function in the dissociation model, while the downstream signaling routes of Mayo have yet to be uncovered. Of note, non-dissociative TA-dependent signaling has also been observed for several aGPCRs[60,63–67] and may occur independently or in parallel to dissociative aGPCR signals.[59,68] Reduced heart rates in *mayo*$^{-\Delta GPS+1}$ mutants, in which the putative TA of Mayo is affected by the mutagenesis, imply that Mayo may also signal through this paradigm.

mayo is expressed in the larval midgut and the anal pads,[29] which are involved in ion absorption.[69,70] Interestingly, we found that the number of ECs in *mayo*^{KO} larvae is increased, while other lineages and anal pads appeared undisturbed. This is interesting, as the larval midgut is thought to grow in size not by constant production of ECs, but by genome endoduplication and volume increases per individual EC,[71] suggesting that *mayo* is

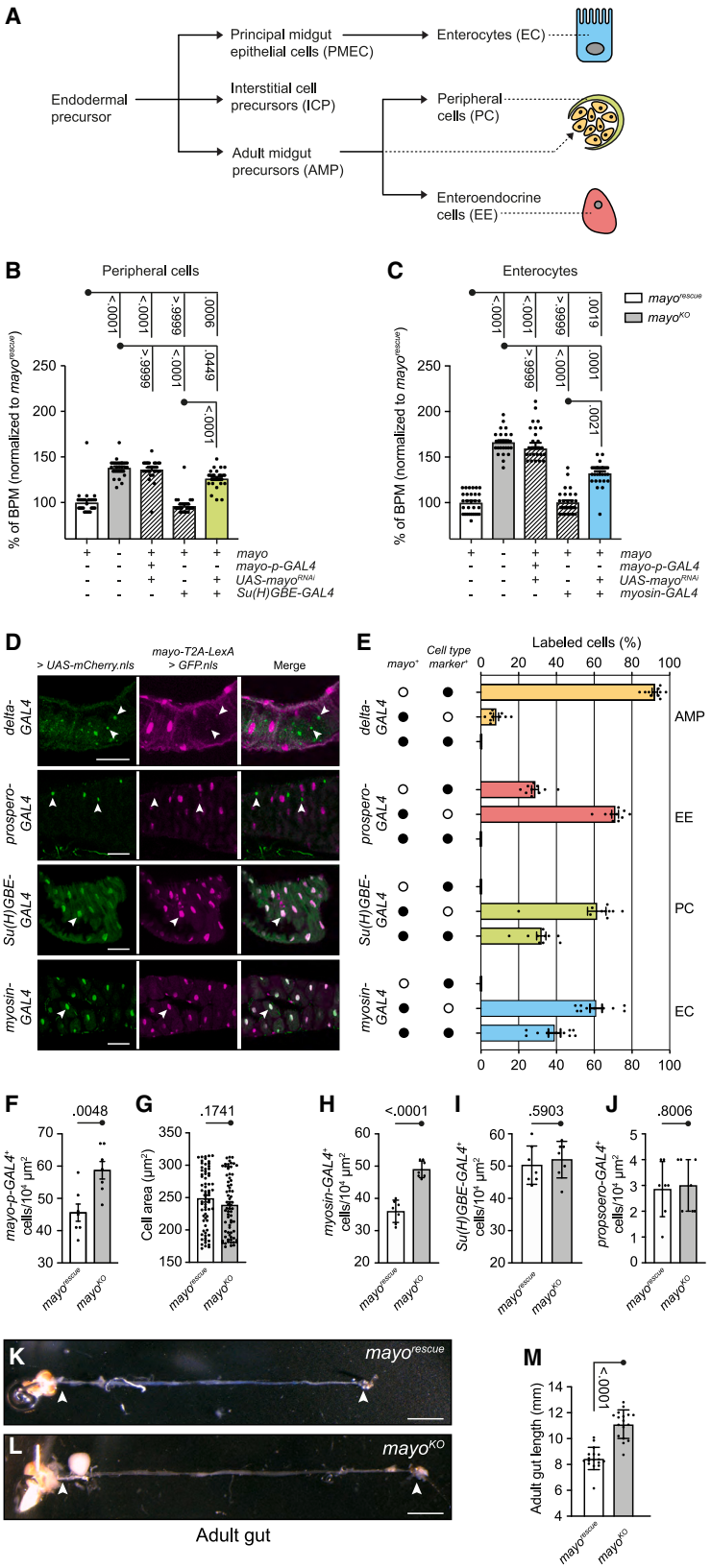

Figure 4. *mayo* controls PC and EC number and larval midgut size

(A) Lineage relationship of larval midgut cell types tested for *mayo* requirement.[5] Color scheme is used in quantification diagrams.

(B and C) Selective removal of *mayo* from PCs (D) and ECs (E) phenocopies $mayo^{KO}$ tachycardia. See also Figures S3E and S3F.

(D) Confocal images of *mayo-T2A-LexA* reporter with different enteric lineage markers. Arrowheads indicate cells that are positive for the respective lineage marker. Scale bars: 50 µm.

(E) Quantification of cells expressing *mayo-T2A-LexA* with or without cell-type markers shown in (A). Colors correspond to lineages shown in (A). Empty circles correspond to the absence of *mayo* or cell marker, and black circles correspond to the presence of *mayo* and/or the cell marker.

(F) Quantification of *mayo-p-GAL4*$^+$ cells in a defined larval midgut area of 10^4 µm^2.

(G) Quantification of *mayo-p-GAL4*$^+$ cell sizes, based on maximum projections of confocal images, in a defined larval midgut area of 10^4 µm^2.

(H–J) Quantification of *mayo*$^+$ *myosin-GAL4*$^+$ larval ECs (H) and PCs (I) and *mayo*$^-$ *prospero-GAL4*$^+$ EEs (J) in $mayo^{rescue}$ and $mayo^{KO}$ L3 larval midgut.

(K and L) Representative guts dissected out of $mayo^{rescue}$ (K) and $mayo^{KO}$ adults (L). Arrowheads mark anatomical landmarks for length measurements. Scale bars: 1 mm.

(M) Quantification of adult gut lengths. Data are shown as mean ± SD.

All data are shown as mean ± SEM if not indicated otherwise.

an important factor for preventing the production of ancillary larval ECs under normal conditions. *mayo* resulted in a selective increase of *myosin-GAL4*$^{+}$ ECs, arguing that *mayo* physiologically suppresses proliferation in the PMEC-EC lineage. This is in line with previous results that found *mayo* as one of more than a dozen genes whose knockdown resulted in increased intestinal stem cells (ISC)/enteroblasts (EB) abundance in adult flies.[72]

Interestingly, several other aGPCRs have proliferative activities including ADGRG6/Gpr126 in Schwann cells,[73] ADGRG1/Gpr56 in neural progenitor cells,[74] ADGRB1/BAI1 in endothelial cells,[75] and ADGRB2/BAI2 in hippocampal neurons.[76] The function of *mayo* may therefore contribute to the control over asymmetric mitotic activity of PMECs to yield a fixed EC pool. As previously shown, the aGPCR Cirl exerts a similar effect to adjust the number of neuroblasts in the larval brain of *Drosophila melanogaster*,[30] and its homolog LAT-1 controls mitotic spindle positioning and division planes of early blastomeres in *C. elegans*.[77]

Also, adult guts of *mayo*^{KO} flies were elongated. A similar phenotype was reported after overexpression of CD97/ADGRE5 in mouse intestinal epithelial cells, which caused a mega-intestine through cylindrical growth, showing that aGPCRs partake in GI development in other species too.[78]

In order to clarify which cell type relies on *mayo* function, we harnessed the observation that *mayo*^{KO} larvae display a marked non-cell-autonomous tachycardia likely caused by a mild hyperkalemia. This is in line with the role of K^+ currents in the repolarization of the *Drosophila* heart, while Na^+ does not affect the heart frequency in *Drosophila*.[40,79] Further, cardiac action potentials in invertebrates are carried by K^+ and Ca^{2+} fluxes,[80] and K^+ channel mutations can cause cardiac arrhythmias,[81,82] confirming the involvement of K^+ channels in the regulation of the cardiac pacemaker.

We utilized the tachycardia in *mayo*^{KO} larvae in a screen to test which cells require *mayo* autonomously to maintain physiological K^+ hemolymph levels. Only removal of *mayo* from PCs and ECs resulted in tachycardiac frequencies, showing that *mayo* is not only expressed but also required in those cells for the maintenance of a normal cardiac heart frequency.[83]

Limitations of the study

The first characterization of the aGPCR *mayo* in *Drosophila* has provided insights into its role in the larval midgut as a potential mitotic suppressor at the PMEC-EC transition. Future studies will need to clarify which molecular function *mayo* serves in ECs and PCs and how it does so. To this end, it is necessary to determine Mayo ligands and intracellular signaling conduits to reconstruct the receptor's signaling pathway. In particular, how Mayo is integrated into the mechanisms of EC proliferation will be of prime interest. This will shed light on how removal of *mayo* causes an increase in EC number and whether its mode of action is comparable to effects of other aGPCRs on mitotic activity, cell polarity, division, and fate determination.[30,73,77,83–89]

In conjunction with the proliferative effect of *mayo* removal on ECs we conclude that this cell type likely affects K^+ uptake into the hemolymph either directly through ion channels or transporters/exchange proteins,[90] or indirectly by controlling the abundance of enteric cell types that express them. Thus, future work needs to address whether the extracellular potassium concentration simply scales with the EC number, or whether *mayo* impacts potassium flux phenomena in ECs as well.

STAR★METHODS

Detailed methods are provided in the online version of this paper and include the following:

- KEY RESOURCES TABLE
- RESOURCE AVAILABILITY
  - Lead contact
  - Materials availability
  - Data and code availability
- EXPERIMENTAL MODEL AND STUDY PARTICIPANT DETAILS
  - Drosophila stock and culture
- METHOD DETAILS
  - Molecular reagents
  - Structural predictions of the mayo GAIN domain
  - Heart frequency quantification
  - anti-RFP immunostainings
  - Cell size measurement and number quantification
  - Gut length measurement
  - Osmolality measurement
  - Protein extraction, purification and Western blot
  - Electrophysiological hemolymph potassium concentration measurements
- QUANTIFICATION AND STATISTICAL ANALYSIS

SUPPLEMENTAL INFORMATION

Supplemental information can be found online at https://doi.org/10.1016/j.celrep.2023.113640.

ACKNOWLEDGMENTS

This work was supported by grants of the Deutsche Forschungsgemeinschaft (DFG) to N.S. and T.L. through FOR2149, project P01 (project number 265903901), and CRC 1423, project B06 (project number 421152132), to P.W.H. (CRC 1423, project C01) and to W.H. (HU 2474/1-1). N.S., D.L. and B.B.-R. were supported through Junior research grants from the Faculty of Medicine, Leipzig University. We thank Mikio Furuse, Bruno Lemaitre, Nicolas Buchon, and Jonas Messner for sharing plasmids, antibodies, and protocols. Transgenic fly stocks and/or plasmids were obtained from the Vienna Drosophila Resource Center (VDRC) and from the Bloomington Drosophila Stock Center (NIH P40OD018537). Publication costs were partially covered by the Open Access Publishing (OAP) fund of Leipzig University supported by the DFG OAP funding program.

AUTHOR CONTRIBUTIONS

F.V.C. designed, performed, and analyzed experiments; created manuscript figures; and wrote the manuscript. G.M.A. designed, performed, and analyzed experiments. L.M. performed and analyzed experiments. V.R. performed and analyzed experiments. W.H. identified genetic tools. F.S. performed computational protein structure prediction, compared GAIN domains, and contributed to manuscript figures. P.W.H. supervised the *in silico* part of the manuscript. N.S. performed and analyzed experiments. A.S.T. designed and analyzed experiments and identified genetic tools. D.L. designed, performed, and analyzed experiments. B.B.-R. initiated the study; designed, performed and analyzed experiments; and wrote the manuscript. T.L. initiated the study,

designed and analyzed experiments, created manuscript figures, and wrote the manuscript.

DECLARATION OF INTERESTS

The authors declare no competing interests.

Received: March 2, 2023
Revised: November 14, 2023
Accepted: December 16, 2023

REFERENCES

1. Naikkhwah, W., and O'Donnell, M.J. (2012). Phenotypic plasticity in response to dietary salt stress: Na+ and K+ transport by the gut of Drosophila melanogaster larvae. J. Exp. Biol. *215*, 461–470.
2. Buchon, N., Osman, D., David, F.P.A., Fang, H.Y., Boquete, J.-P., Deplancke, B., and Lemaitre, B. (2013). Morphological and Molecular Characterization of Adult Midgut Compartmentalization in Drosophila. Cell Rep. *3*, 1725–1738.
3. Miguel-Aliaga, I., Jasper, H., and Lemaitre, B. (2018). Anatomy and Physiology of the Digestive Tract of Drosophila melanogaster. Genetics *210*, 357–396.
4. Tian, A., Benchabane, H., and Ahmed, Y. (2018). Wingless/Wnt Signaling in Intestinal Development, Homeostasis, Regeneration and Tumorigenesis: A Drosophila Perspective. J. Dev. Biol. *6*, 8.
5. Chen, J., and St Johnston, D. (2022). Epithelial Cell Polarity During Drosophila Midgut Development. Front. Cell Dev. Biol. *10*, 886773.
6. Mathur, D., Bost, A., Driver, I., and Ohlstein, B. (2010). A Transient Niche Regulates the Specification of Drosophila Intestinal Stem Cells. Science *327*, 210–213.
7. Dutta, D., Dobson, A.J., Houtz, P.L., Gläßer, C., Revah, J., Korzelius, J., Patel, P.H., Edgar, B.A., and Buchon, N. (2015). Regional Cell-Specific Transcriptome Mapping Reveals Regulatory Complexity in the Adult Drosophila Midgut. Cell Rep. *12*, 346–358.
8. Hung, R.-J., Hu, Y., Kirchner, R., Liu, Y., Xu, C., Comjean, A., Tattikota, S.G., Li, F., Song, W., Ho Sui, S., and Perrimon, N. (2020). A cell atlas of the adult Drosophila midgut. Proc. Natl. Acad. Sci. USA *117*, 1514–1523.
9. Biteau, B., Karpac, J., Supoyo, S., DeGennaro, M., Lehmann, R., and Jasper, H. (2010). Lifespan Extension by Preserving Proliferative Homeostasis in Drosophila. PLoS Genet. *6*, e1001159.
10. de Navascués, J., Perdigoto, C.N., Bian, Y., Schneider, M.H., Bardin, A.J., Martínez-Arias, A., and Simons, B.D. (2012). Drosophila midgut homeostasis involves neutral competition between symmetrically dividing intestinal stem cells. EMBO J. *31*, 2473–2485.
11. Lemaitre, B., and Miguel-Aliaga, I. (2013). The Digestive Tract of Drosophila melanogaster. Annu. Rev. Genet. *47*, 377–404.
12. Marianes, A., and Spradling, A.C. (2013). Physiological and stem cell compartmentalization within the Drosophila midgut. Elife *2*, e00886.
13. Hamann, J., Aust, G., Araç, D., Engel, F.B., Formstone, C., Fredriksson, R., Hall, R.A., Harty, B.L., Kirchhoff, C., Knapp, B., et al. (2015). International Union of Basic and Clinical Pharmacology. XCIV. Adhesion G Protein–Coupled Receptors. Pharmacol. Rev. *67*, 338–367.
14. Kan, Z., Jaiswal, B.S., Stinson, J., Janakiraman, V., Bhatt, D., Stern, H.M., Yue, P., Haverty, P.M., Bourgon, R., Zheng, J., et al. (2010). Diverse somatic mutation patterns and pathway alterations in human cancers. Nature *466*, 869–873.
15. Zhu, D., Osuka, S., Zhang, Z., Reichert, Z.R., Yang, L., Kanemura, Y., Jiang, Y., You, S., Zhang, H., Devi, N.S., et al. (2018). BAI1 Suppresses Medulloblastoma Formation by Protecting p53 from Mdm2-Mediated Degradation. Cancer Cell *33*, 1004–1016.e5.
16. Langenhan, T., Piao, X., and Monk, K.R. (2016). Adhesion G protein-coupled receptors in nervous system development and disease. Nat. Rev. Neurosci. *17*, 550–561.
17. Folts, C.J., Giera, S., Li, T., and Piao, X. (2019). Adhesion G Protein-Coupled Receptors as Drug Targets for Neurological Diseases. Trends Pharmacol. Sci. *40*, 278–293.
18. Vitobello, A., Mazel, B., Lelianova, V.G., Zangrandi, A., Petitto, E., Suckling, J., Salpietro, V., Meyer, R., Elbracht, M., Kurth, I., et al. (2022). ADGRL1 haploinsufficiency causes a variable spectrum of neurodevelopmental disorders in humans and alters synaptic activity and behavior in a mouse model. Am. J. Hum. Genet. *109*, 1436–1457.
19. Chang, G.-W., Hsiao, C.-C., Peng, Y.-M., Vieira Braga, F.A., Kragten, N.A.M., Remmerswaal, E.B.M., van de Garde, M.D.B., Straussberg, R., König, G.M., Kostenis, E., et al. (2016). The Adhesion G Protein-Coupled Receptor GPR56/ADGRG1 Is an Inhibitory Receptor on Human NK Cells. Cell Rep. *15*, 1757–1770.
20. Boyden, S.E., Desai, A., Cruse, G., Young, M.L., Bolan, H.C., Scott, L.M., Eisch, A.R., Long, R.D., Lee, C.-C.R., Satorius, C.L., et al. (2016). Vibratory Urticaria Associated with a Missense Variant in ADGRE2. N. Engl. J. Med. *374*, 656–663.
21. Scholz, N., Langenhan, T., and Schöneberg, T. (2019). Revisiting the classification of adhesion GPCRs. Ann Ny Acad Sci *1456*, 80–95.
22. Kelley, L.A., and Sternberg, M.J.E. (2009). Protein structure prediction on the Web: a case study using the Phyre server. Nat. Protoc. *4*, 363–371.
23. McGuffin, L.J., Bryson, K., and Jones, D.T. (2000). The PSIPRED protein structure prediction server. Bioinformatics *16*, 404–405.
24. Jumper, J., Evans, R., Pritzel, A., Green, T., Figurnov, M., Ronneberger, O., Tunyasuvunakool, K., Bates, R., Žídek, A., Potapenko, A., et al. (2021). Highly accurate protein structure prediction with AlphaFold. Nature *596*, 583–589.
25. van Kempen, M., Kim, S.S., Tumescheit, C., Mirdita, M., Lee, J., Gilchrist, C.L.M., Söding, J., and Steinegger, M. (2023). Fast and accurate protein structure search with Foldseek. Nat. Biotechnol., 1–4.
26. Araç, D., Boucard, A.A., Bolliger, M.F., Nguyen, J., Soltis, S.M., Südhof, T.C., and Brunger, A.T. (2012). A novel evolutionarily conserved domain of cell-adhesion GPCRs mediates autoproteolysis. EMBO J. *31*, 1364–1378.
27. Vizurraga, A., Adhikari, R., Yeung, J., Yu, M., and Tall, G.G. (2020). Mechanisms of adhesion G protein–coupled receptor activation. J. Biol. Chem. *295*, 14065–14083.
28. Nieberler, M., Kittel, R.J., Petrenko, A.G., Lin, H.-H., and Langenhan, T. (2016). Control of Adhesion GPCR Function Through Proteolytic Processing. Handb. Exp. Pharmacol. *234*, 83–109.
29. Blanco-Redondo, B., and Langenhan, T. (2018). Parallel Genomic Engineering of Two Drosophila Genes Using Orthogonal attB/attP Sites. G3 (Bethesda). *8, g3*, 3109–3118.
30. Scholz, N., Dahse, A.-K., Kemkemer, M., Bormann, A., Auger, G.M., Vieira Contreras, F., Ernst, L.F., Staake, H., Körner, M.B., Buhlan, M., et al. (2023). Molecular sensing of mechano- and ligand-dependent adhesion GPCR dissociation. Nature *615*, 945–953.
31. Brunet Avalos, C., Maier, G.L., Bruggmann, R., and Sprecher, S.G. (2019). Single cell transcriptome atlas of the Drosophila larval brain. Elife *8*, e50354.
32. Krause, S.A., Overend, G., Dow, J.A.T., and Leader, D.P. (2022). FlyAtlas 2 in 2022: enhancements to the Drosophila melanogaster expression atlas. Nucleic Acids Res. *50*, D1010–D1015.
33. Deng, B., Li, Q., Liu, X., Cao, Y., Li, B., Qian, Y., Xu, R., Mao, R., Zhou, E., Zhang, W., et al. (2019). Chemoconnectomics: Mapping Chemical Transmission in Drosophila. Neuron *101*, 876–893.e4.
34. Bour, B.A., O'Brien, M.A., Lockwood, W.L., Goldstein, E.S., Bodmer, R., Taghert, P.H., Abmayr, S.M., and Nguyen, H.T. (1995). Drosophila MEF2, a transcription factor that is essential for myogenesis. Gene Dev. *9*, 730–741.

35. Drechsler, M., Schmidt, A.C., Meyer, H., and Paululat, A. (2013). The Conserved ADAMTS-like Protein Lonely heart Mediates Matrix Formation and Cardiac Tissue Integrity. PLoS Genet. *9*, e1003616.

36. Han, Z., Yi, P., Li, X., and Olson, E.N. (2006). Hand, an evolutionarily conserved bHLH transcription factor required for Drosophila cardiogenesis and hematopoiesis. Development *133*, 1175–1182.

37. Izumi, Y., Furuse, K., and Furuse, M. (2019). Septate junctions regulate gut homeostasis through regulation of stem cell proliferation and enterocyte behavior in Drosophila. J. Cell Sci. *132*, jcs232108.

38. Zhang, F., Zhao, Y., and Han, Z. (2013). An In Vivo Functional Analysis System for Renal Gene Discovery in Drosophila Pericardial Nephrocytes. J. Am. Soc. Nephrol. *24*, 191–197.

39. Sellin, J., Albrecht, S., Kölsch, V., and Paululat, A. (2006). Dynamics of heart differentiation, visualized utilizing heart enhancer elements of the Drosophila melanogaster bHLH transcription factor Hand. Gene Expr. Patterns *6*, 360–375.

40. Gu, G.G., and Singh, S. (1995). Pharmacological analysis of heartbeat in Drosophila. J. Neurobiol. *28*, 269–280.

41. Sénatore, S., Rami Reddy, V., Sémériva, M., Perrin, L., and Lalevée, N. (2010). Response to Mechanical Stress Is Mediated by the TRPA Channel Painless in the Drosophila Heart. PLoS Genet. *6*, e1001088.

42. Lalevée, N., Monier, B., Sénatore, S., Perrin, L., and Sémériva, M. (2006). Control of Cardiac Rhythm by ORK1, a Drosophila Two-Pore Domain Potassium Channel. Curr. Biol. *16*, 1502–1508.

43. Johnson, E., Ringo, J., Bray, N., and Dowse, H. (1998). Genetic and Pharmacological Identification of Ion Channels Central to the Drosophila Cardiac Pacemaker. J. Neurogenet. *12*, 1–24.

44. Singh, A., and Singh, S. (1999). Unmasking of a Novel Potassium Current in Drosophila by a Mutation and Drugs. J. Neurosci. *19*, 6838–6843.

45. Krans, J.L., Parfitt, K.D., Gawera, K.D., Rivlin, P.K., and Hoy, R.R. (2010). The resting membrane potential of Drosophila melanogaster larval muscle depends strongly on external calcium concentration. J. Insect Physiol. *56*, 304–313.

46. Olsson, T., MacMillan, H.A., Nyberg, N., Staerk, D., Malmendal, A., and Overgaard, J. (2016). Hemolymph metabolites and osmolality are tightly linked to cold tolerance of Drosophila species: a comparative study. J. Exp. Biol. *219*, 2504–2513.

47. Dietzl, G., Chen, D., Schnorrer, F., Su, K.-C., Barinova, Y., Fellner, M., Gasser, B., Kinsey, K., Oppel, S., Scheiblauer, S., et al. (2007). A genome-wide transgenic RNAi library for conditional gene inactivation in Drosophila. Nature *448*, 151–156.

48. Kvon, E.Z., Kazmar, T., Stampfel, G., Yáñez-Cuna, J.O., Pagani, M., Schernhuber, K., Dickson, B.J., and Stark, A. (2014). Genome-scale functional characterization of Drosophila developmental enhancers in vivo. Nature *512*, 91–95.

49. Jiang, H., and Edgar, B.A. (2009). EGFR signaling regulates the proliferation of Drosophila adult midgut progenitors. Development *136*, 483–493.

50. Huang, H.-W., Zeng, X., Rhim, T., Ron, D., and Ryoo, H.D. (2017). The requirement of IRE1 and XBP1 in resolving physiological stress during Drosophila development. J. Cell Sci. *130*, 3040–3049.

51. Phillips, M.D., and Thomas, C.M. (2006). Brush border spectrin is required for early endosome recycling in Drosophila. J. Cell Sci. *119*, 1361–1370.

52. Tepass, U., and Hartenstein, V. (1995). Neurogenic and proneural genes control cell fate specification in the Drosophila endoderm. Development *121*, 393–405.

53. Takashima, S., Younossi-Hartenstein, A., Ortiz, P.A., and Hartenstein, V. (2011). A novel tissue in an established model system: the Drosophila pupal midgut. Dev. Genes Evol. *221*, 69–81.

54. Kimbrell, D.A., Hice, C., Bolduc, C., Kleinhesselink, K., and Beckingham, K. (2002). The Dorothy enhancer has tinman binding sites and drives hopscotch-induced tumor formation. Genesis *34*, 23–28.

55. Ponzielli, R., Astier, M., Chartier, A., Gallet, A., Thérond, P., and Sémériva, M. (2002). Heart tube patterning in Drosophila requires integration of axial and segmental information provided by the Bithorax Complex genes and hedgehog signaling. Development *129*, 4509–4521.

56. Purcell, R.H., and Hall, R.A. (2018). Adhesion G Protein–Coupled Receptors as Drug Targets. Annu. Rev. Pharmacol. *58*, 429–449.

57. Langenhan, T., Aust, G., and Hamann, J. (2013). Sticky Signaling—Adhesion Class G Protein–Coupled Receptors Take the Stage. Sci. Signal. *6*, re3. re3–re3.

58. Yeung, J., Adili, R., Stringham, E.N., Luo, R., Vizurraga, A., Rosselli-Murai, L.K., Stoveken, H.M., Yu, M., Piao, X., Holinstat, M., and Tall, G.G. (2020). GPR56/ADGRG1 is a platelet collagen-responsive GPCR and hemostatic sensor of shear force. Proc. Natl. Acad. Sci. USA *117*, 28275–28286.

59. Frenster, J.D., Stephan, G., Ravn-Boess, N., Bready, D., Wilcox, J., Kieslich, B., Wilde, C., Sträter, N., Wiggin, G.R., Liebscher, I., et al. (2021). Functional impact of intramolecular cleavage and dissociation of adhesion G protein–coupled receptor GPR133 (ADGRD1) on canonical signaling. J. Biol. Chem. *296*, 100798.

60. Liu, D., Duan, L., Rodda, L.B., Lu, E., Xu, Y., An, J., Qiu, L., Liu, F., Looney, M.R., Yang, Z., et al. (2022). CD97 promotes spleen dendritic cell homeostasis through the mechanosensing of red blood cells. Science *375*, eabi5965.

61. Karpus, O.N., Veninga, H., Hoek, R.M., Flierman, D., van Buul, J.D., vandenAkker, C.C., vanBavel, E., Medof, M.E., van Lier, R.A.W., Reedquist, K.A., and Hamann, J. (2013). Shear Stress–Dependent Downregulation of the Adhesion-G Protein–Coupled Receptor CD97 on Circulating Leukocytes upon Contact with Its Ligand CD55. J. Immunol. *190*, 3740–3748.

62. Bassilana, F., Nash, M., and Ludwig, M.-G. (2019). Adhesion G protein-coupled receptors: opportunities for drug discovery. Nat. Rev. Drug Discov. *18*, 869–884.

63. Prömel, S., Frickenhaus, M., Hughes, S., Mestek, L., Staunton, D., Woollard, A., Vakonakis, I., Schöneberg, T., Schnabel, R., Russ, A.P., and Langenhan, T. (2012). The GPS Motif Is a Molecular Switch for Bimodal Activities of Adhesion Class G Protein-Coupled Receptors. Cell Rep. *2*, 321–331.

64. Scholz, N., Guan, C., Nieberler, M., Grotemeyer, A., Maiellaro, I., Gao, S., Beck, S., Pawlak, M., Sauer, M., Asan, E., et al. (2017). Mechano-dependent signaling by Latrophilin/CIRL quenches cAMP in proprioceptive neurons. Elife *6*, e28360.

65. Sando, R., Jiang, X., and Südhof, T.C. (2019). Latrophilin GPCRs direct synapse specificity by coincident binding of FLRTs and teneurins. Science *363*, eaav7969.

66. Liebscher, I., Schön, J., Petersen, S.C., Fischer, L., Auerbach, N., Demberg, L.M., Mogha, A., Cöster, M., Simon, K.-U., Rothemund, S., et al. (2014). A Tethered Agonist within the Ectodomain Activates the Adhesion G Protein-Coupled Receptors GPR126 and GPR133. Cell Rep. *9*, 2018–2026. –2026.

67. Bohnekamp, J., and Schöneberg, T. (2011). Cell Adhesion Receptor GPR133 Couples to Gs Protein. J. Biol. Chem. *286*, 41912–41916.

68. Kishore, A., Purcell, R.H., Nassiri-Toosi, Z., and Hall, R.A. (2016). Stalk-dependent and Stalk-independent Signaling by the Adhesion G Protein-coupled Receptors GPR56 (ADGRG1) and BAI1 (ADGRB1). J. Biol. Chem. *291*, 3385–3394.

69. Jarial, M.S. (1987). Ultrastructure of the anal organ of Drosophila larva with reference to ion transport. Tissue Cell *19*, 559–575.

70. Flower, N.E., and Walker, G.D. (1979). Rectal papillae in Musca domestica: the cuticle and lateral membranes. J. Cell Sci. *39*, 167–186.

71. Houtz, P., Bonfini, A., Bing, X., and Buchon, N. (2019). Recruitment of Adult Precursor Cells Underlies Limited Repair of the Infected Larval Midgut in Drosophila. Cell Host Microbe *26*, 412–425.e5.

72. Xu, C., Franklin, B., Tang, H.-W., Regimbald-Dumas, Y., Hu, Y., Ramos, J., Bosch, J.A., Villalta, C., He, X., and Perrimon, N. (2020). An in vivo RNAi screen uncovers the role of AdoR signaling and adenosine deaminase in

controlling intestinal stem cell activity. Proc. Natl. Acad. Sci. USA *117*, 464–471.

73. Mogha, A., Benesh, A.E., Patra, C., Engel, F.B., Schöneberg, T., Liebscher, I., and Monk, K.R. (2013). Gpr126 Functions in Schwann Cells to Control Differentiation and Myelination via G-Protein Activation. J. Neurosci. *33*, 17976–17985.
74. Bae, B.-I., Tietjen, I., Atabay, K.D., Evrony, G.D., Johnson, M.B., Asare, E., Wang, P.P., Murayama, A.Y., Im, K., Lisgo, S.N., et al. (2014). Evolutionarily Dynamic Alternative Splicing of GPR56 Regulates Regional Cerebral Cortical Patterning, *343* (New York, NY: Science), pp. 764–768.
75. Koh, J.T., Kook, H., Kee, H.J., Seo, Y.-W., Jeong, B.C., Lee, J.H., Kim, M.-Y., Yoon, K.C., Jung, S., and Kim, K.K. (2004). Extracellular fragment of brain-specific angiogenesis inhibitor 1 suppresses endothelial cell proliferation by blocking alphavbeta5 integrin. Exp. Cell Res. *294*, 172–184.
76. Okajima, D., Kudo, G., and Yokota, H. (2011). Antidepressant-like behavior in brain-specific angiogenesis inhibitor 2-deficient mice. J. Physiol. Sci. *61*, 47–54.
77. Langenhan, T., Prömel, S., Mestek, L., Esmaeili, B., Waller-Evans, H., Hennig, C., Kohara, Y., Avery, L., Vakonakis, I., Schnabel, R., and Russ, A.P. (2009). Latrophilin signaling links anterior-posterior tissue polarity and oriented cell divisions in the C. elegans embryo. Dev. Cell *17*, 494–504.
78. Aust, G., Kerner, C., Gonsior, S., Sittig, D., Schneider, H., Buske, P., Scholz, M., Dietrich, N., Oldenburg, S., Karpus, O.N., et al. (2013). Mice overexpressing CD97 in intestinal epithelial cells provide a unique model for mammalian postnatal intestinal cylindrical growth. Mol. Biol. Cell *24*, 2256–2268.
79. Singh, S., and Wu, C.-F. (1989). Complete separation of four potassium currents in drosophila. Neuron *2*, 1325–1329.
80. Johnson, E., Sherry, T., Ringo, J., and Dowse, H. (2002). Modulation of the cardiac pacemaker of Drosophila: cellular mechanisms. J. Comp. Physiol. B *172*, 227–236.
81. Ocorr, K., Perrin, L., Lim, H.-Y., Qian, L., Wu, X., and Bodmer, R. (2007). Genetic Control of Heart Function and Aging in Drosophila. Trends Cardiovas Med *17*, 177–182.
82. Liu, X.W., Wu, H.M., Bai, Y., Zeng, Q., Cao, Z.M., Wu, X.S., and Tang, M. (2021). Potassium channel Shaker play a protective role against cardiac aging in Drosophila. Yi Chuan Hered *43*, 94–99.
83. Nishimura, T., Honda, H., and Takeichi, M. (2012). Planar cell polarity links axes of spatial dynamics in neural-tube closure. Cell *149*, 1084–1097.
84. Usui, T., Shima, Y., Shimada, Y., Hirano, S., Burgess, R.W., Schwarz, T.L., Takeichi, M., and Uemura, T. (1999). Flamingo, a Seven-Pass Transmembrane Cadherin, Regulates Planar Cell Polarity under the Control of Frizzled. Cell *98*, 585–595.
85. Müller, A., Winkler, J., Fiedler, F., Sastradihardja, T., Binder, C., Schnabel, R., Kungel, J., Rothemund, S., Hennig, C., Schöneberg, T., and Prömel, S. (2015). Oriented Cell Division in the C. elegans Embryo Is Coordinated by G-Protein Signaling Dependent on the Adhesion GPCR LAT-1. PLoS Genet. *11*, e1005624.
86. Strutt, H., Warrington, S., Madathil, A.C.K., Langenhan, T., and Strutt, D. (2023). Molecular symmetry breaking in the Frizzled-dependent planar polarity pathway. Curr. Biol. *33*, 5340–5354.e6.
87. Warrington, S.J., Strutt, H., and Strutt, D. (2013). The Frizzled-dependent planar polarity pathway locally promotes E-cadherin turnover via recruitment of RhoGEF2 *140*, 1045–1054.
88. Doyle, S.E., Scholz, M.J., Greer, K.A., Hubbard, A.D., Darnell, D.K., Antin, P.B., Klewer, S.E., and Runyan, R.B. (2006). Latrophilin-2 is a novel component of the epithelial-mesenchymal transition within the atrioventricular canal of the embryonic chicken heart. Dev. Dynam. *235*, 3213–3221.
89. Monk, K.R., Naylor, S.G., Glenn, T.D., Mercurio, S., Perlin, J.R., Dominguez, C., Moens, C.B., and Talbot, W.S. (2009). A G protein-coupled receptor is essential for Schwann cells to initiate myelination. Science (New York, NY *325*, 1402–1405.
90. Overend, G., Luo, Y., Henderson, L., Douglas, A.E., Davies, S.A., and Dow, J.A.T. (2016). Molecular mechanism and functional significance of acid generation in the Drosophila midgut. Sci. Rep. *6*, 27242.
91. Han, Z., and Olson, E.N. (2005). Hand is a direct target of Tinman and GATA factors during Drosophila cardiogenesis and hematopoiesis. Development *132*, 3525–3536.
92. Schneider, C.A., Rasband, W.S., and Eliceiri, K.W. (2012). NIH Image to ImageJ: 25 years of image analysis. Nat. Methods *9*, 671–675.
93. Kelley, L.A., Mezulis, S., Yates, C.M., Wass, M.N., and Sternberg, M.J.E. (2015). The Phyre2 web portal for protein modeling, prediction and analysis. Nat. Protoc. *10*, 845–858.
94. Frishman, D., and Argos, P. (1995). Knowledge-based protein secondary structure assignment. Proteins *23*, 566–579.
95. Pfeiffer, B.D., Ngo, T.-T.B., Hibbard, K.L., Murphy, C., Jenett, A., Truman, J.W., and Rubin, G.M. (2010). Refinement of Tools for Targeted Gene Expression in Drosophila. Genetics *186*, 735–755.
96. Octeau, J.C., Faas, G., Mody, I., and Khakh, B.S. (2018). Making, Testing, and Using Potassium Ion Selective Microelectrodes in Tissue Slices of Adult Brain. J. Vis. Exp. *10*.
97. McCann, F.V. (1965). Unique properties of the moth myocardium. Ann Ny Acad Sci *127*, 84–99.

STAR★METHODS

KEY RESOURCES TABLE

REAGENT or RESOURCE	SOURCE	IDENTIFIER
Antibodies		
Rabbit-α-RFP	Antibodies-Online	Cat#ABIN129578; RRID: AB_10781500
Alexa Fluor 488 conjugated goat-α-Rabbit	Thermo Fisher	Cat#A11008; RRID: AB_143165
Mouse-α-tubulinb	DSHB	Cat#e7;RRID: AB_528499
IRDye 680RD goat-α-rabbit	LI-COR	RRID:AB_2721181
IRDye 680RD goat-α-mouse	LI-COR	RRID:AB_2651128
800CW goat-α-mouse	LI-COR	RRID:AB_2687825
800CW goat-α-rabbit	LI-COR	RRID:AB_2651127
Bacterial and virus strains		
XL1-Blue Competent Cells	Agilent	Cat#200236
NEB® 5-alpha Competent E. coli (High Efficiency)	NEB	C2987I
Chemicals, peptides, and recombinant proteins		
4x Protein Sample Loading Buffer	LI-COR	Cat#928-4004
Protease Inhibitor Cocktail	Sigma Aldrich	Cat#P2714
Odyssey Blocking Buffer	LI-COR	Cat#927-70001
5% dichlorodimethylsilane	Sigma	Cat#85126
valinomycin	Sigma	Cat#60403
1,2-Dimethyl-3-nitrobenzene	Sigma	Cat#40870
Potassium-tetrakis-(4-chlorophenyl)-borate	Sigma	Cat#60591
Critical commercial assays		
ChromoTek RFP-Trap Magnetic Agarose kit	Proteintech	Cat#rtmak
NEBuilder® HiFi DNA Assembly Cloning Kit	NEB	Cat#E5520S
Experimental models: Organisms/strains		
D. melanogaster: *mRFP-mayo: w^{1118}; +; $attP^{TT}${mRFP-mayo 3xP3-DsRed^{-}[pTL855]}$mayo^{KO}$;+*	This paper	N/A
D. melanogaster: *$mayo^{KO}$-p-Gal4: w^{1118}; +; $attP^{TT}${$mayo^{KO}$-p-GAL4 3xP3-DsRed^{-}[pBB6]}$mayo^{KO}$;+*	This paper	N/A
D. melanogaster: *$mayo^{KO}$: w^{1118}; +; $attP^{TT}$ $loxP^{+}$ $mayo^{KO}$ 3xP3-DsRed^{-};+*	(Blanco-Redondo and Langenhan, 2018)[29]	N/A
D. melanogaster: $mayo^{Rescue}$: w^{1118}; +; $attP^{TT}${CG11318-rescue 3xP3-DsRed^{-}[pTL784]}$mayo^{KO}$;+	(Blanco-Redondo and Langenhan, 2018)[29]	N/A
D. melanogaster: $mayo^{\Delta GPS-2(H>A)}$: w[1118];+; CG11318[1]{attP-TT + loxP+}[3P>DsRed-], att{Mayo H>A(pTL860) [3xP3-DsRed-]}[attPmayo]/TM3, Sb	This paper	N/A
D. melanogaster: $mayo^{\Delta GPS+1(T>A)}$: w[1118];+; CG11318[1]{attP-TT + loxP+}[3P>DsRed-], att{Mayo T>A(pTL861) [3xP3-DsRed-]}[attPmayo]/TM3, Sb	This paper	N/A
D. melanogaster: $mayo^{\Delta GPS-2(H>A)}$-NRS-LexA: w[1118]; +; CG11318[1]{attP-TT + loxP+}[3P>DsRed-] [attB-mayo(H>A)-NRS-LexA DsRed- (pTL915)]/TM3,Sb;	(Scholz et al., 2023)[30]	N/A
D. melanogaster: $mayo^{\Delta GPS+1(T>A)}$-NRS-LexA: w[1118]; +; CG11318[1]{attP-TT + loxP+}[3P>DsRed-] [attB-mayo(T>A)-NRS-LexA DsRed- (pTL916)]/TM3,Sb;	This paper	N/A
D. melanogaster: mayo-p-Gal4: w^{1118}; +; $attP^{TT}${mayo-p-GAL4 3xP3-DsRed^{-}[pTL789]}$mayo^{KO}$;+	(Blanco-Redondo and Langenhan, 2018)[29]	N/A
D. melanogaster: mayo-T2A-LexA: w; +; TI{2A-lexA::p65}CG11318[2A-lexA]*	Bloomington Drosophila Stock Center	RRID:BDSC_84366

(*Continued on next page*)

Continued

REAGENT or RESOURCE	SOURCE	IDENTIFIER
D. melanogaster: myo-GAL4: w[*]; P{w[+mW.hs]=GawB}Myo31DF[NP0001]/CyO; +	Bloomington Drosophila Stock Center	RRID:BDSC_67088
D. melanogaster: UAS-RNAi against *CG11318= UAS-mayo^{RNAi}: w^{1118};P[GD705]V3395*	FlyBase	RRID:FlyBase_FBst0460392
D. melanogaster: UAS-RNAi against *CG11318: w^{1118};P[KK1056685]^{v108136}*	(Dietzl et al., 2007)[47]	N/A
D. melanogaster: Df(3R)Exel7379: w^{1118};Df(3R)Exel7379/TM6B, Tb	Bloomington Drosophila Stock Center	RRID:BDSC_7919
D. melanogaster: Vienna Tile-GAL4 line expressed in anal pad cells*(analpad-GAL4):*	Bloomington Drosophila Stock Center	RRID:BDSC_73162
D. melanogaster: Vienna Tile-GAL4 line expressed in anal pad cells: *w^{1118};;VT-045245-Gal4*	(Kvon et al., 2014)[48]	N/A
D. melanogaster: Vienna Tile-GAL4 line expressed in anal pad cells: *w^{1118};;VT-034308-Gal4*	(Kvon et al., 2014)[48]	N/A
D. melanogaster: Hand-GAL4: Hand-GAL4 w^{+}	(Han and Olson, 2005)[91]	N/A
D. melanogaster: mef2-GAL4: w;+;P{w^{+m*}=Mef2-GAL4.247}^{3}*	Bloomington Drosophila Stock Center	RRID:BDSC_50742
D. melanogaster: mex-GAL4: w^{1118}; TM2, P{w^{+mC}=mex1-GAL4.2.1}12-8/TM6B, Tb^{1}	Bloomington Drosophila Stock Center	RRID:BDSC_91369
D. melanogaster: tin-GAL4: w; P{w$^{+mW.hs}$}=tin-Gal4.B}2*	Bloomington Drosophila Stock Center	RRID:BDSC_91538
*D. melanogaster: dot-GAL4: P{w^{+mC}=Ugt36A1-GAL4.K}^{43A}, y^{1} w**	Bloomington Drosophila Stock Center	RRID:BDSC_6903
D. melanogaster: delta-GAL4: w^{1118}; P{w^{+mC} =UAS-3xFLAG.dCas9.VPR}^{attP40}/CyO; P{w$^{+mC.hs}$ =GawB}Dl$^{05151-G}$, P{w^{+mC} =tubP-GAL80^{ts}}2/TM6B, Tb^{1}	Bloomington Drosophila Stock Center	RRID:BDSC_67047
D. melanogaster: Su(H)-GAL4: w; P{w^{+mC} =Su(H)GBE-GAL4}^{2}/CyO*	Bloomington Drosophila Stock Center	RRID:BDSC_83377
D. melanogaster: LexAop-GFP.nls: w^{1118};+;P{w^{+m*}=lexAop-2xhrGFP.nls}^{3a}	Bloomington Drosophila Stock Center	RRID:BDSC 29955
D. melanogaster: LexAop-GFP.nls: w^{1118};P{w^{+m*}=lexAop-2xhrGFP.nls}^{3a}	Bloomington Drosophila Stock Center	RRID:BDSC 29954
D. melanogaster: 20xUAS-6xGFP: y^{1} w; wg [Sp-1]/CyO, P{Wee-P.ph0}Bacc [Wee-P20]; P{y$^{+t7.7}$ w^{+mC}=20XUAS-6XGFP}^{attP2}*	Bloomington Drosophila Stock Center	RRID:BDSC 52262
D. melanogaster: UAS-mCherry.nls: w;P{w^{+mC}=UAS-mCherry.nls}^{3}*	Bloomington Drosophila Stock Center	RRID:BDSC 38424
D. melanogaster: UAS-mCherry.nls: w;P{w[+mC]=UAS-mCherry.nls}^{2};MKRS/TM6B, Tb^{1}*	Bloomington Drosophila Stock Center	RRID:BDSC 38425
Oligonucleotides		
Mayo genotyping tl_631F: ttgaagcttactaaattgaagcc	This paper	N/A
Mayo genotyping tl_632R: tatgaaatgcaaagcacttcacc	This paper	N/A
Mayo genotyping tl_634R: tccagagtgcactttgcggcaga	This paper	N/A
Cloning mayo^{KO}-p-Gal4 bb_46F: agttctagatTCGCGAGGCGCGCCggtac cataacttcgtataatgtatgctatacgaag	This paper	N/A
Cloning mayo^{KO}-p-Gal4 bb_47R: tggtaccGGCGCGCCTCGCGAatctagaac tagtggatctaaacgagtttttaagcaaac	This paper	N/A
Cloning mayo^{KO}-p-Gal4 bb_48F: gctagagttgttgg ttggcacaccacaaatatactgttgccgagcacaattccgctcg	This paper	N/A

(*Continued on next page*)

Continued

REAGENT or RESOURCE	SOURCE	IDENTIFIER
Cloning mayo^{KO}-p-Gal4 bb_49R: ttgtggtgtgccaaccaacaactctagctttgc gtactcgcaaattattaaaaataaaaac	This paper	N/A
Recombinant DNA		
CG11318^{KO}/mayo^{KO} HDR vector	(Blanco-Redondo and Langenhan, 2018)[29]	N/A
CG11318^{Rescue}/mayo^{Rescue} vector	(Blanco-Redondo and Langenhan, 2018)[29]	N/A
mayo-p-GAL4 reporter vector	(Blanco-Redondo and Langenhan, 2018)[29]	N/A
mayo^{KO}-p-GAL4 reporter vector	This paper	N/A
mRFP-mayo vector	This paper	N/A
mayo$^{\Delta GPS-2}$ vector	(Scholz et al., 2023)[30]	N/A
mayo$^{\Delta GPS-+1}$ vector	This paper	N/A
Software and algorithms		
Fiji-ImageJ	(Schneider et al., 2012)[92]	https://ImageJ.nih.gov/ij/
Odyssey Fc 2800	LI-COR	N/A
Clampex software	Molecular Devices	N/A
SigmaPlot 14	Systat	N/A
Prism 7	Graphpad	N/A
PyMOL ver.2.5.0a0	Schrödinger	https://pymol.org/2/
Phyre2 web server	(Kelley et al., 2015)[93]	http://www.sbg.bio.ic.ac.uk/~phyre2/
AlphaFold database	(Jumper et al., 2021)[24]	https://alphafold.ebi.ac.uk/
STRIDE	(Frishman and Argos, 1995)[94]	https://webclu.bio.wzw.tum.de/stride/
Other		
Fluoromount G	Thermo Fisher	Cat#495802
Hoechst 33342	Thermo Fisher	Cat#62249

RESOURCE AVAILABILITY

Lead contact

Further information and requests for resources and reagents should be directed to and will be fulfilled by the lead contact, Tobias Langenhan (tobias.langenhan@gmail.com).

Materials availability

Plasmids are available upon request, fly strains generated in this study will be deposited at the Bloomington Drosophila Stock Center.

Data and code availability

(1) All data are available from the lead author upon request.
(2) This paper does not report original code.
(3) Any additional information required to reanalyze the data reported in this work paper is available from the lead contact upon request.

EXPERIMENTAL MODEL AND STUDY PARTICIPANT DETAILS

Drosophila stock and culture

mayo^{KO} and *mayo^{rescue}* strains were 5x back-crossed to the wildtype *w^{1118}* background before further analyses were conducted to avoid second-site effects.

All flies (key resource table) were reared in the following food: 60% water, 3.4% agar, 9% yeast, 5% soy flour, 40% corn flour, 0.7% nipagin, 9% treacle and 0.52% propionic acid. Flies were kept at 25°C, in 65% humidity and a 12h light/dark cycle. RNAi lines were obtained from the Vienna Drosophila Resource Center (transformant IDs 3395 and 108136) and *esg-GAL4* (67054) and *dot-GAL4*

(6903) from Bloomington Drosophila Stock Center. The *analpad-GAL4* lines were obtained from the Flylight collection, Janelia Research Campus. For the experiments, L3 animals were synchronised and staged by selection of the largest larvae still crawling in the food, but not wandering on the vial walls.

METHOD DETAILS

Molecular reagents

All engineered plasmids (key resource table) were modified using restriction enzymes from New England Biolabs. PCRs were conducted using AccuStarDNA Polymerase (Eurogentec), primers and custom DNA fragments were synthesized by MWG Eurofins or Life Technologies. All intermediate and final constructs were DNA-sequenced to ensure no errors were introduced during the cloning procedures. The template genomic DNA used for PCR amplification throughout the study was from the local stock of the w^{1118} strain (Flybase ID: FBal0018186). All primers used are listed in the key resource table.

CG11318^{KO}/mayo^{KO} *HDR vector*

A 0.9 kb fragment encoding the 59 homology arm was amplified from genomic DNA using primers tl_681F/682R, cut with AarI and inserted into de-phosphorylated AarI-digested pHD- DsRed-attP (pTL645). Subsequently, the 1.2 kb 39 homology arm was PCR-amplified from genomic DNA using primers tl_683F/684R, cut with SapI, and inserted into de-phosphorylated pTL645 to generate the final mayo^{KO} plasmid pTL650 (attP^{+}, *loxP*$^{+}$, dsRed^{+})

CG11318^{Rescue}/mayo^{Rescue} *vector (pTL784)*

A 4.6 kb fragment corresponding exactly to the genomic *CG11318* sequence removed through the CRISPR/Cas9 cuts was amplified off genomic DNA. The DNA fragment was double digested with NotI and AscI and inserted into pGE-attBTT-DsRed to generate the wild-type *CG11318/mayo* rescue plasmid (attP^{+}, *loxP*$^{+}$, dsRed^{+})

mayo-p-GAL4 *reporter vector (pTL789)*

In order to insert a GAL4.2 transcription factor cassette at the transcriptional start site of *CG11318*, a 1.6 kb AgeI/NsiI fragment of pTL784 was subcloned into pTL550 (pMCS5 derivative with KanR; MoBiTec; pTL785). This subclone was outward PCR-amplified using primers tl_824F/tl_825R to generate a 4.6 kb amplicon. An 1.6 kb fragment encoding the optimized GAL4 cassette was amplified off pBPGal4.2:p65d[95] using primers tl_822F/tl_823R. Both PCR fragments were appended with primer-encoded BglII and NheI sites on either end, respectively, digested with BglII/NheIand ligated generating clone pTL787. A 3.2 kb AgeI/NsiI fragment of this clone was re-transferred into the *CG11318* rescue vector pTL784 to construct the final *mayo-p*^{Gal4} reporter allele plasmid pTL789 (attB^{+}, *loxP*$^{+}$, dsRed^{+}).

mayo^{KO}-p-GAL4 *reporter vector (pBB6)*

In order to remove mayo from pTL789, we used the NEBuilder HiFi Assembly technique. The plasmid was PCR-amplified using primers bb_48F/bb_47R to generate a 2.7 kb amplicon and bb_46F/bb_47R to generate a 3.9 kb amplicon missing the genomic *CG11318* sequence. Both PCR fragments were assembled with NEBuilder HiFi to construct the final *mayo*^{KO}*-p-Gal4* reporter vector (attB^{+}, *loxP*$^{+}$, dsRed^{+}).

mRFP-mayo *vector (pTL855)*

The full-length sequence of mRFP was introduced at the N-terminal part of the *mayo* gene including a GGGGG linker sequence at the N- and C-terminal ends of the chromophore. The AA sequence of the final protein is given in Supp Figure S1A. An order was placed on Genscript Gene Synthesis to extract a 672 kb fragment corresponding exactly to the *RFP* sequence present in the vector with internal name pMN4, and subcloned it into the wild-type *CG11318* rescue vector pTL784 containing *mayo*, resulting in the final mRFP::Mayo plasmid pTL855 (attB^{+}, *loxP*$^{+}$, dsRed^{+}).

mayo$^{\Delta GPS-2}$ *(pTL860) and* mayo$^{\Delta GPS-+1}$ *(pTL861) vectors*

Both were synthesized by Genscript using pTL784 as the basis vector for modifications.

All plasmids were verified by Sanger sequencing before fly transgenesis.

Structural predictions of the mayo GAIN domain

For secondary structure prediction, the Phyre2 web server (http://www.sbg.bio.ic.ac.uk/~phyre2/) was used.[93] A truncated sequence of Mayo including the ECD and 7TM region (residues 1–802) and a sequence truncated 15 residues C-terminal of the GPS (residues 1–490) were used as templates for AlphaFold (full database preset, maximum template date 15.02.2022)[24] to predict the structure of the Mayo ECD. The sequences were passed to a local AlphaFold version as a single chain, therefore predicted structures are in an uncleaved state. After checking for significant differences in the models from the two sequences, the secondary structure information was extracted via STRIDE[94] from the best ranked structure, respectively. Protein structure was assessed qualitatively with PyMOL ver.2.5.0a0 and compared to the four existing structures of aGPCR GAIN domains (PDB IDs: 4DLQ, 4DLO, 5KVM, 6V55).

Heart frequency quantification

L3 larvae were collected from the food and placed for 1 min individually in an equal volume (enough to cover the larvae) of fresh, room temperature HL-3.3 solution (70 mM NaCl, 0.5 mM $MgCl_2$, 5 mM KCl, 5 mM Saccharose, 115 mM Sucrose and 5 mM HEPES) in a 96-well plate. After 1 min, the larva was then removed from the HL-3.3 solution, positioned with the ventral area facing up, where the

heartbeat is best observed, onto a dry black sylgard dissecting stage, and placed under the stereo microscope with a 1.6x (objective) times 10× (ocular) magnification. The larvae were handled throughout the experiment with blunt ended tweezers.

For kymographic analysis larval heart activity was recorded in MP4 format with a digital camera (MC190HD, Leica) mounted on a Leica MZ10 F stereo microscope. Movie file frames were exported with Adobe Photoshop v22.4.2 as individual images in PNG-format, and loaded as an image series in Fiji/ImageJ2 v2.3.0. Kymographs were generated along a line perpendicularly placed over the larval heart diameter using the Multi Kymograph ImageJ-plugin v3.0.1 by Reitdorf, Seitz, Schindelin (https://imagej.net/imagej-wiki-static/Multi_Kymograph).

For manual quantification the number of beats was counted for 10 s and the heart frequency was calculated. This procedure was done with one larva at a time and repeated until the required number of larvae were measured. Any time the heart was not readily observable under the microscope, the value was not included into the analysis. For the quantification after an exposure to a pharmacological inhibitor, normal heart frequency was measured as described above and larvae were then put back into a solution with the inhibitor. Heart frequency was then quantified under the microscope as described for the unchallenged larvae.

anti-RFP immunostainings

Drosophila L3 larvae were selected and dissected in ice-cold minimal hemolymph-like solution (HL3 medium), guts were removed and fixed for 30 min at room temperature in 4% paraformaldehyde (PFA). Guts were washed in 1X PBS, blocked for 1 h at room temperature in 0.3% Triton X-100 in PBS, unless otherwise stated, containing 5% normal goat serum (Jackson Immunology, Philadelphia, USA), and then incubated overnight at 4°C in the primary antibody [rabbit-α-RFP (1:200, Antibodies-Online #ABIN129578; RRID: AB_10781500)] with constant agitation. The next day the samples were washed 3 × 20 min in 0.3% Triton X-100 in PBS with 5% normal goat serum and then incubated for 2 h with the secondary antibody [Alexa Fluor 488 conjugated goat-α-Rabbit (1:250, details #A11008; RRID: AB_143165)] and Hoechst 33342 20 mM (Thermo Scientific Catalog #62249) at room temperature with constant agitation. Following a final 3 × 20 min wash in 0.3% Triton X-100 in PBS the guts were then mounted in Fluoromount G, purchased from Thermo Fischer Scientific (Massachusetts, USA), on a Menzel-Gläser glass slide from Thermo Fischer Scientific and covered with Menzel-Gläser glass coverslip (both Menzel-Gläser, Thermo Fischer Scientific, Massachusetts, USA) for fluorescence microscopy. The mounts were examined using a LEICA SP8 Confocal Microscope and analyzed in Fiji-ImageJ (NIH).

Cell size measurement and number quantification

Guts were dissected from L3 larvae, treated with 4% PFA for 1 h and washed 3 × 10 min with PBS each. The guts were mounted with one spacer between the slide and the coverslip. Images were obtained with a confocal microscope using the 20x magnification. All other settings were maintained equal between samples. Cell sizes and numbers in a midgut area of 0.01 mm^2 were then quantified with ImageJ. Only the cells with co-localization of the nuclei and DAPI in a midgut area of 0.01 mm^2 were quantified.

Gut length measurement

Larvae or adults were incubated with a solution of 1/1 Blue Coomassie and yeast for 1 h. Upon ingestion, this mixture resulted in a blue stained midgut that was used as guide. Guts were dissected from L3 larvae and adults from the posterior area, without detaching the anterior part, e.g., the foregut from the head. Subsequently, a picture of the straightened gut was taken with a Leica MZ 10F microscope. Gut length was then measured with ImageJ in pixels using the line tool and subsequently converted into mm.

Osmolality measurement

Larvae of each genotype were individually collected from food. An incision was made by using a glass micro pipette pulled with the DMZ universal electrode puller from Zeitz which provides electrodes with outer diameters of approx. 0.8 μm. This diameter is only illustrative, as long as the electrode is sharp enough to create a small incision in the larval epidermis, there is no need for a precise tip diameter. Special care was taken not to rupture any internal organs during larval epidermis puncture. From the small incision, the hemolymph would flow out and was collected with a 1 μL pipette tip and quickly transferred to a measuring paper, which absorbed the liquid. This measuring paper was then introduced into the osmometer (Vapro Vapor Pressure Osmometer model 5600; Elitech Group Biomedical Systems) to measure the overall osmolality.

Protein extraction, purification and Western blot

Fly pupae were collected into 1.5 mL Eppendorf tube and mechanical homogenization in a N_2 precooled mortar was applied, the powder was mixed with 2 mL of Lysis Buffer (Chromotek) supplemented with protease Inhibitor Cocktail, Sigma-Aldrich (1:1000) and transferred into a 5 mL tube. Homogenization with IKA T10 basic ULTRA-TURRAX was applied 4 × 15 s each. The sample was transferred into 2 mL Eppendorf tube and centrifuged at 4°C for 30 min with 4000 rpm with Eppendorf Centrifuge 5415R with a fixed angle rotor FA 45 24 11. The supernatant was transferred into a new tube and centrifuged again at 4°C for 30 min with 13000 rpm. The supernatant was again collected into 1.5 mL Eppendorf tube and centrifuged at 4°C for 30 min with 25000 rpm using a Sigma 3-30KS Sartorius with a fixed angle rotor 30x1.5/2 mL 3–16 3-16K 3–30 K L 3–18. One aliquot of the supernatant was saved for analysis. 75 μL of Immunomagnetic RFP beads (Chromotek) were transferred into 1.5 mL tube and washed 3 times with 500 μL wash buffer (Chromotek), the supernatant was added on each tube and incubated at 4°C for 2 h with end-over-end rotation. Next, the supernatant was collected and an aliquot was kept for analysis. The beads were washed three times with 500 μL wash buffer

(Chromotek). 50 μL of 2x SDS sample buffer (LI-COR) supplemented with β-Mercaptoethanol was added to the beads and incubated at 95°C for 10 min. The beads were separated and the supernatant was kept for Wester blotting.

The samples were subjected to electrophoresis on 4–12% Tris-Glycin SDS gel (Novex-Wedge-Well; Invitrogen) and blotted onto nitrocellulose membrane (0.2 μm pore size). The membrane was blocked for 1 h (RT) using Odyssey Blocking buffer (LI-COR) diluted 1:1 with 1x PBS.

Blots were probed with primary antisera at the indicated concentrations overnight at 4°C: rabbit-α-RFP (1:1000; RRID:AB_10781500), mouse-α-tubulinb (1:5000, DSHB e7; RRID: AB_528499). After rinsing twice and 3 × 10 min washing steps, membranes were incubated with IRDye 680RD goat-α-rabbit (RRID:AB_2721181) and goat-α-mouse (RRID:AB_2651128) as well as 800CW goat-α-mouse (1:15000; RRID:AB_2687825) and goat-α-rabbit (1:15000; RRID:AB_2651127) for 1 h at RT, and again rinsed twice and washed for 3 × 10 min. Blots were imaged with an OdysseyFc 2800 (LI-COR).

Electrophysiological hemolymph potassium concentration measurements

To measure hemolymph K^+ concentrations, we recorded potentials (voltages) between a K^+ selective electrode and a reference electrode, which were both dipped into hemolymph of *Drosophila* larvae. Potentials were recorded, using the Axoclamp 900A amplifier, the Axon Digidata 1550B analog-digital converter and Clampex software (all three from Molecular Devices). The experimenter was blinded to the genotypes during measurements and analysis. To make potassium-selective electrodes we were guided by the protocols in.[96] Filament-less glass capillaries (Science Products, GB150-8P) were washed in 1 M HCl overnight, rinsed in 70% ethanol, dried for 6–8 h at 100°C–120°C and stored in an air tight container alongside anhydrous $CaSO_4$ desiccant (Drierite, 23001) for up to four weeks. Prior to salinization (i.e., making the glass surface hydrophobic), the capillaries were pulled with the DMZ universal electrode puller (Zeitz) to micro-pipettes with outer diameters of 17.4μm ± 3.3 (SD) and of 17.3μm ± 2.9 (SD) for measurements in $mayo^{rescue}$ and in $mayo^{KO}$ animals, respectively. The micro-pipettes were salinized by applying drops of a 5% dichlorodimethylsilane (Sigma 85126) to both ends of the micro-pipettes and by heating them to 210°C for 45–60 min. They were stored in the same air tight container for up to one week. The ionophore cocktail, which was used to induce K^+ selectivity, contained 50 mg valinomycin (Sigma 60403), 20 mg Potassium-tetrakis-(4-chlorophenyl)-borate (Sigma 60591) and 930 μL 1,2-Dimethyl-3-nitrobenzene (Sigma 40870). The micropipettes were first back-filled with 10 μL of 100 mM KCl. The solution was pushed into the pipette tip by applying pressure to the rear opening of the electrode. A drop of the ionophore cocktail was applied to the tip of the micropipette under microscopic control to front-fill the pipette to 0.9–1.1 mm by capillary forces. To calculate K^+ concentrations from the voltage measured in the hemolymph, the potential between the K^+ electrode and the Ag/AgCl reference electrode was recorded in calibration solutions, which contained 1, 10 and 100 mM KCl. The 1 and 10 mM KCl solutions additionally contained LiCl to match the osmotic pressure of the 100 mM KCl solution. In order to not contaminate the small volume of hemolymph with calibration solution, both, the sharp reference electrode and the K^+ electrode were briefly rinsed in ddH_20 and dried. A female L3 non-wandering larva was washed, dried and immobilized with the dorsal side up, using transparent scotch tape (Figure 3F). The K^+ selective electrode and the sharp Ag/AgCl reference electrode were placed slightly above the scotch tape along the body midline at around 1/3 body length away from the posterior end. A voltage recording (∼1 min long) was started, then the scotch tape together with the larval body wall were impaled with a sharp insect pin (Fine Science Tools, 26002-10), while sparing the internal organs. A drop of hemolymph formed on the scotch tape surface. The electrode tips were quickly immersed (within 3 s) in the drop of hemolymph solution. K^+ selective electrodes were discarded after one measurement. The measured potential dropped quickly after the immersion of the electrodes, but after a few seconds, probably due to hemolymph evaporation, started to increase, thus increasing apparent K^+ concentration. Therefore, we used the average voltage within 2 s around the lowest values as a measure of the voltage. This occurred usually within the first 10 s of the recording. A linear regression function, $V = \text{slope} * \lg(c_{K+}) + V_0$ (V, measured voltage; $c_K{}^+$, potassium concentration in the calibration solution; V_0, intercept with the y axis), was fitted to the voltages at three different lg of K^+ concentrations in the calibration solution (0, 1 and 2, i.e., 1 mM, 10 mM and 100 mM repectively, Figure 3G) to determine the slope and the y axis intercept V_0 (Figure 3G). With these values and the voltage, measured in the hemolymph, the corresponding K^+ concentration in hemolymph was calculated using an analogous formula. For lack of the value of the intracellular K^+ concentration in *Drosophila melanogaster*, the Nernst equation was solved using $[K^+]_{in} = -88.0$ mV obtained in the moth *Samia cecropia*[97] at T = 291 K.

QUANTIFICATION AND STATISTICAL ANALYSIS

Data presented as mean with ± SEM from at least three independent experiments. Data distribution was initially tested with a Shapiro-Wilk test for normal distribution. Two-set comparisons were performed with two-tailed unpaired t test (for normally distributed samples) or Mann-Whitney U test (for non-normally distributed samples). Multiple comparison analyses of >2 datasets were conducted with ordinary one-way ANOVA followed by Tukey's multiple comparison test (for normally distributed samples), or Kruskal-Wallis test followed by Dunn's multiple comparison test (for non-normally distributed samples). Corresponding p-values are presented in each figure. Data analysis and statistical comparisons for the electrophysiological measurements were performed in SigmaPlot 14 (Systat), data were plotted using Prism 7 (GraphPad).

Data presented in the figures were statistically assessed as indicated (normality test/comparison test):

Figure 2B: Kolmogorov-Smirnov / unpaired two-tailed t-test

Figure 2C: *mayo*$^{\Delta GPS-2}$ dataset: Kolmogorov-Smirnov / ordinary one-way ANOVA and a Tukey's multiple comparisons test; *mayo*$^{\Delta GPS+1}$ dataset: Kolmogorov-Smirnov / Kruskal-Wallis and Dunn's multiple comparison tests
Figure 3A,B: Kolmogorov-Smirnov / paired two-tailed t-test
Figure 3C,D: Kolmogorov-Smirnov / Kruskal-Wallis and Dunn's multiple comparison tests
Figure 3E: Kolmogorov-Smirnov / unpaired two-tailed t-test
Figure 3H: Kolmogorov-/ Mann-Whitney U test
Figure 4B,C: Kolmogorov-/ Kruskal-Wallis and Dunn's multiple comparison tests
Figure 4F: Kolmogorov-Smirnov / unpaired two-tailed t-test
Figure 4G: Kolmogorov-Smirnov / Mann-Whitney U test
Figure 4H-J: Kolmogorov-Smirnov / unpaired two-tailed t-test
Figure 4M: Kolmogorov-Smirnov / unpaired two-tailed t-test
Figure S1B: Kolmogorov-Smirnov / unpaired two-tailed t-test
Figure S1C: Kolmogorov-/ Kruskal-Wallis and Dunn's multiple comparison tests
Figure S1D: Kolmogorov-Smirnov / Kruskal-Wallis and Dunn's multiple comparison tests
Figure S1F: Kolmogorov-Smirnov / Kruskal-Wallis and Dunn's multiple comparison tests
Figure S2A,B: Kolmogorov-Smirnov / Dunn's multiple comparison test
Figure 3A,C,E-J: Kolmogorov-Smirnov / Dunn's multiple comparison test